

A COMPREHENSIVE X-RAY AND MULTIWAVELENGTH STUDY OF THE COLLIDING GALAXY PAIR NGC 2207/IC 2163

S. MINEO^{1,2}, S. RAPPAPORT^{3,6}, A. LEVINE⁴, D. POOLEY^{5,6}, B. STEINHORN⁷, & J. HOMAN⁴

Draft version October 14, 2014

ABSTRACT

We present a comprehensive study of the total X-ray emission from the colliding galaxy pair NGC 2207/IC 2163, based on *Chandra*, *Spitzer*, and *GALEX* data. We detect 28 ultra-luminous X-ray sources (‘ULXs’), 7 of which were not detected previously due to X-ray variability. Twelve sources show significant long-term variability, with no correlated spectral changes. Seven sources are transient candidates. One ULX coincides with an extremely blue star cluster (B-V = -0.7). We confirm that the global relation between the number and luminosity of ULXs and the integrated star formation rate (‘SFR’) of the host galaxy also holds on *local* scales. We investigate the effects of dust extinction and/or age on the X-ray binary (‘XRB’) population on sub-galactic scales. The distributions of N_X and L_X are peaked at $L_{IR}/L_{NUV} \sim 1$, which may be associated with an age of ~ 10 Myr for the underlying stellar population. We find that $\sim 1/3$ of the XRBs are located in close proximity to young star complexes. The luminosity function of the X-ray binaries (‘XRBs’) is consistent with that typical for high-mass X-ray binaries, and appears unaffected by variability. We disentangle and compare the X-ray diffuse spectrum with that of the bright XRBs. The hot interstellar medium dominates the diffuse X-ray emission at $E \lesssim 1$ keV, has a temperature $kT = 0.28^{+0.05}_{-0.04}$ keV and intrinsic 0.5-2 keV luminosity of 7.9×10^{40} erg s⁻¹, a factor of ~ 2.3 higher than the average thermal luminosity produced per unit SFR in local star-forming galaxies. The total X-ray output of NGC 2207/IC 2163 is 1.5×10^{41} erg s⁻¹, and the corresponding total integrated SFR is $23.7 M_\odot$ yr⁻¹.

Subject headings: stars: binaries: general — stars: formation — stars: luminosity function, mass function — stars: neutron — galaxies: individual (NGC 2207/IC 2163) — galaxies: interactions — galaxies: starburst — (ISM:) dust, extinction — X-rays: binaries — X-rays: ISM — infrared: galaxies

1. INTRODUCTION

Galaxies in collision are known to host intense star formation activity. Presumably this is due to dynamical shocks that are induced by the supersonic relative speeds of the galaxies in comparison to the thermal speeds of the stars and gas clouds within the galaxies. These shocks, in turn, trigger the collapse of molecular clouds, leading to the formation of star clusters with a wide spectrum of stellar masses, including O and B stars (Struck 1997; Struck et al. 2005; Bonnell et al. 2006). Furthermore, as is well known empirically, many of these O and B stars will naturally be found in binary systems.

Accompanying these star formation events in galaxy collisions are the production of numerous different classes

of high-energy astrophysical objects such as core-collapse supernovae (Hamuy et al. 2000; Konishi et al. 2011); high-mass X-ray binaries (HMXBs; David et al. 1992; Grimm et al. 2003; Swartz et al. 2004; Liu et al. 2006); and gamma-ray burst sources (Bloom et al. 2002). In the case of HMXBs and gamma-ray burst sources, binary stars are an intrinsic part of the evolution of these objects (see, e.g., Bhattacharya & van den Heuvel 1991; Woosley & Heger 2012), and they may also be relevant to the evolution of many supernovae (see, e.g., Podsiadlowski et al. 1993), both core collapse and thermonuclear events. In general, the more massive star in the binary evolves first, may lose its envelope via mass transfer and/or ejection from the system, and this is followed by the collapse of the core which produces either a black hole or neutron star. When that collapsed star accretes matter from the original secondary in the system, either via stellar wind accretion or Roche-lobe overflow, a massive X-ray binary is formed.

Among the many HMXBs that are found in collisional galaxies, a small fraction ($\sim 10\%$, according to Mineo et al. 2012a) are so-called “ultraluminous X-ray sources” (ULXs). These consist of off-nuclear sources with $L_X > 10^{39}$ erg s⁻¹, a luminosity which corresponds to the Eddington limit for an accreting $10 M_\odot$ black hole and is taken as a fiducial reference point. It is not known exactly what mass of black holes may power ULXs, but both super-Eddington accretion onto stellar-mass black holes (see, e.g., Done & Gierliński 2003; Madhusudhan et al. 2008; Gladstone et al. 2009) and sub-Eddington

¹ Harvard-Smithsonian Center for Astrophysics, 60 Garden Street Cambridge, MA 02138 USA; smineo@cfa.harvard.edu

² Max Planck Institut für Astrophysik, Karl-Schwarzschild-Str. 1 85741 Garching, Germany

³ 37-602B, M.I.T. Department of Physics and Kavli Institute for Astrophysics and Space Research, 70 Vassar St., Cambridge, MA, 02139; sar@mit.edu

⁴ M.I.T. Kavli Institute for Astrophysics and Space Research, Room 37-575, 70 Vassar St., Cambridge, MA, 02139; aml@space.mit.edu; jeroen@space.mit.edu

⁵ Sam Houston State University, Department of Physics, Farrington Building, Suite 204, Huntsville, Texas 77341, dave@shsu.edu

⁶ Eureka Scientific, Inc., 2452 Delmer Street, Suite 100, Oakland, CA 94602

⁷ Harvard-MIT Division of Health Sciences and Technology, Harvard Medical School, 260 Longwood Avenue, Boston, MA 02115; bsteinho@mit.edu

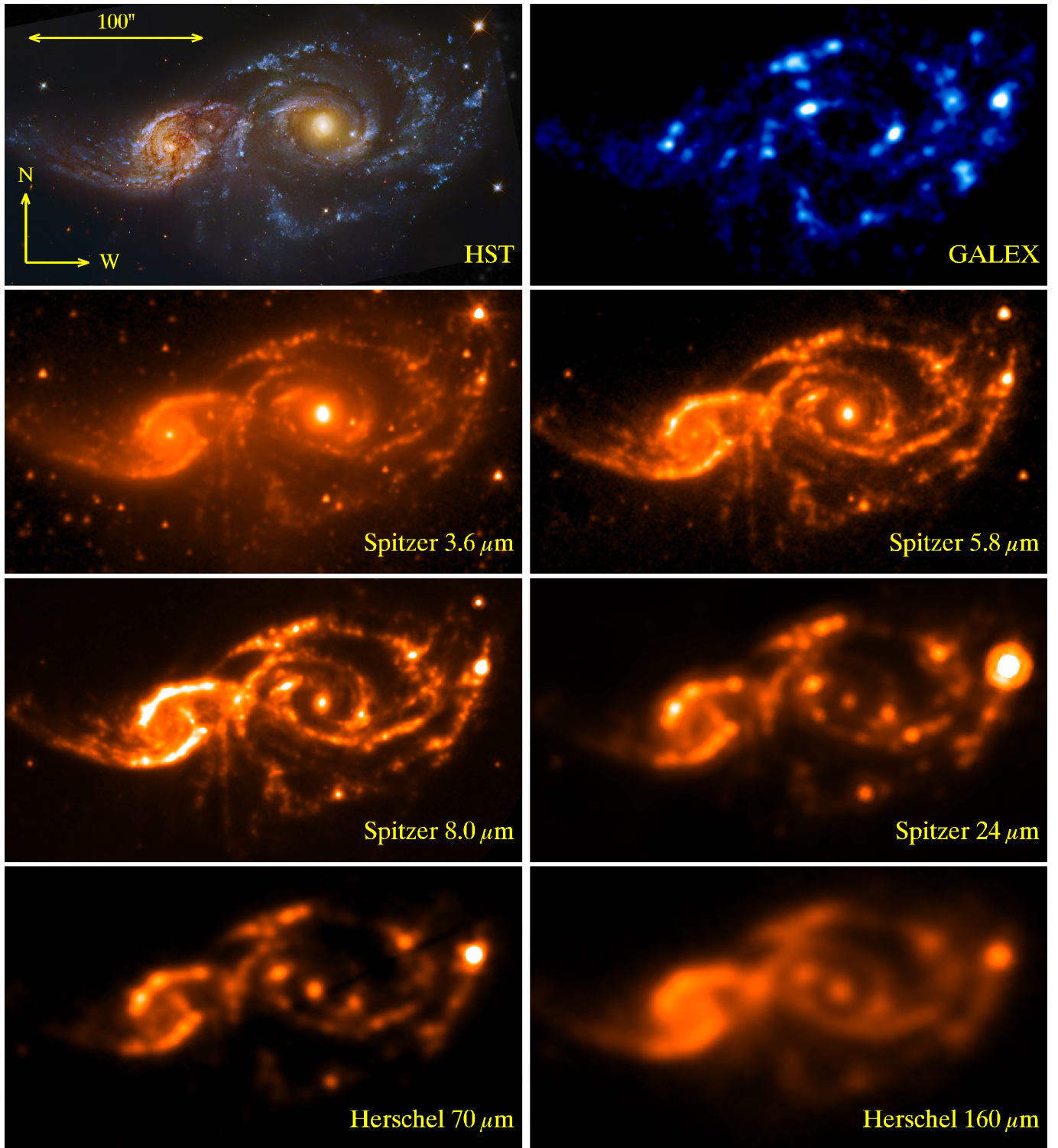


FIG. 1.— Montage of images of NGC 2207/IC 2163 taken with *HST* (WFPC2 camera using filters F336W, F439W, F555W and F814W Elmegreen et al. 2000), *GALEX* (FUV), *Spitzer* (3.6, 5.8, 8.0 and 24 μm), and *Herschel* (70 and 160 μm). NGC 2207 is the larger galaxy on the right.

accretion onto intermediate mass black holes (‘IMBHs’, with masses in the range of $10^3 - 10^4 M_\odot$; Colbert & Mushotzky 1999; Farrell et al. 2009) have been discussed and are plausible⁸ (see Feng & Soria 2011, for a review).

On average $\sim 30\%$ of the ULXs hosted by star-forming galaxies have $L_X > 4 - 5 \times 10^{39} \text{ erg s}^{-1}$ and $\sim 10\%$ are very luminous ($L_X > 10^{40} \text{ erg s}^{-1}$). Many of the high-luminosity ULXs are hosted by colliding galaxies and become X-ray bright $\approx 10\text{--}20 \text{ Myr}$ after the end of star formation (Swartz et al. 2004, 2009; Walton et al. 2011).

The donor stars for most ULXs, i.e., for ULXs hosted by star-forming galaxies, are massive young stars and may be either blue supergiants (Roberts et al. 2001; Liu et al. 2002; Smith et al. 2012), Wolf-Rayet stars (Liu et al. 2013) or red supergiants (Copperwheat et al. 2005; Patruno & Zampieri 2008; Heida et al. 2014).

There are now numerous collisional galaxies that are known to host a substantial number of ULXs (see, e.g. Smith et al. 2012). These include the famous Antennae galaxies (Whitmore & Schweizer 1995; Zezas & Fabbiano 2002), the spectacular Cartwheel galaxy with its prominent “spoke”-like features (Higdon 1995; Gao et al. 2003; Wolter et al. 2006), the “cigar” galaxy M82 (Kaaret et al. 2004), and the more recently studied NGC 2207/IC 2163 (Mineo et al. 2013).

There is a well-established correlation between the total star formation rate (‘SFR’) in a galaxy and the total number of luminous X-rays sources harbored by that galaxy (see, e.g., Grimm et al. 2003; Smith et al. 2005; Mapelli et al. 2010; Swartz et al. 2011; Mineo et al. 2012a). There are numerous different techniques for determining the SFRs which include using separately, or in combination, UV continuum, H α recombination lines, forbidden lines ([O II]), FIR continuum, and thermal radio emission (see, e.g., Kennicutt 1998; Kennicutt & Evans 2012, for detailed discussions). It has been suggested by a number of researchers that an appropriate linear combination of the *GALEX* UV and *Spitzer* FIR bands may be an especially robust indicator of SFR in nearby and starburst galaxies (e.g., Bell 2003; Hirashita et al. 2003; Iglesias-Páramo et al. 2004, 2006; Hao et al. 2011; Kennicutt & Evans 2012). In particular, Leroy et al. (2008) proposed a formulation for computing the SFR based on a specific linear combination of *GALEX* FUV (centered at 1575 Å) and *Spitzer* 24 μm fluxes to enable the creation of spatially-resolved (at the few arc-sec level) images of SFR per unit area (see specifically their Eqns. (D10) and (D11)).

In our previous work on this subject (Mineo et al. 2013) we developed a new approach toward investigating the correlation between the number and luminosity densities of luminous X-ray binaries and the local SFR in the regions immediately surrounding the X-ray sources, using the Leroy et al. (2008) prescription. This novel technique enables us to probe these correlations on a galaxy-by-galaxy basis. In this approach we quantitatively compare the location of the luminous X-ray sources imaged with *Chandra* with the spatial structures in the SFR images. Furthermore, as has been suggested by Calzetti et al. (2005, 2007), Kennicutt & Evans (2012), M. Krumholz

2012, private communication; S. Rappaport et al. 2014, in preparation, the UV fluxes detected by *GALEX* tend to indicate older regions of star formation ($\sim 10\text{--}50 \text{ Myr}$), after the embedded dust has been mostly cleared, in contrast with the 24- μm *Spitzer* images that highlight more recent star formation (i.e., $\sim 5\text{--}10 \text{ Myr}$) where the regions are still enshrouded by dust. These latter regions may harbor more ULXs at the upper end of the luminosity function (i.e., with $L_X \gtrsim 10^{40} \text{ ergs s}^{-1}$). This kind of correlation analysis, done on the local level, enables some of the theoretical ideas concerning the formation and evolution of very massive binaries to be constrained.

Recent results by Luangtip et al. (2014) show that in a sample of 17 nearby ($< 60 \text{ Mpc}$) luminous infrared galaxies (LIRGs) with SFRs $> 7 M_\odot \text{ yr}^{-1}$ and low foreground Galactic column densities ($N_H \lesssim 5 \times 10^{20} \text{ cm}^{-2}$) there is a large deficit (a factor of ~ 10) in the number of ULXs detected per unit SFR when compared to the detection rate in nearby normal star-forming galaxies. The study is based on *Chandra* observations with sufficiently sensitive imaging to permit the detection of all ULXs present in the galaxy. The authors suggest that it is likely that the high column of gas and dust in these galaxies, which fuels the high SFR, also acts to obscure many ULXs from our view.

Based on a sample of Arp interacting galaxies, Smith et al. (2012), found a deficiency of ULXs in the most infrared-luminous galaxies, in agreement with the results mentioned above. They conclude that, although the active galactic nuclei may contribute to powering the far-infrared, ULXs in these galaxies may be highly obscured and therefore not detected by *Chandra*.

On the other hand, Basu-Zych et al. (2013a,b) show that the total X-ray luminosity output per unit SFR in distant star-forming galaxies weakly evolves with redshift. They suggest that the L_X/SFR evolution is driven by metallicity (see also Mapelli et al. 2010; Prestwich et al. 2013; Brorby et al. 2014, for similar conclusions on nearby galaxies), and show that the dust extinction ($L_{\text{IR}}/L_{\text{UV}}$) has insignificant effects on the observed values of L_X/SFR . These results seem consistent with that found by Mineo et al. (2012a), who investigated the correlation of $L_{\text{IR}}/L_{\text{NUV}}$ with $L_X - \text{SFR}$ for HMXBs. They found no correlation, although the average L_X/SFR seems to be decreasing with increasing values of $L_{\text{IR}}/L_{\text{NUV}}$ (see their Fig. 11d).

Our prior analysis of a 13 ks *Chandra* observation of NGC 2207/IC 2163 (Mineo et al. 2013), an impressive pair of spiral galaxies in the initial stages of collision, revealed a total of 21 ULXs within the D25 ellipse (de Vaucouleurs et al. 1991). Such a production efficiency of luminous X-ray sources per unit stellar mass is comparable with that of the Antennae pair of colliding galaxies (Zezas & Fabbiano 2002). Because NGC 2207/IC 2163 turned out to be so rich in ULXs, based on an initially short 13 ks observation (Mineo et al. 2013; see also Kaufman et al. 2012), we were granted three further *Chandra* observations (for a collective additional exposure time of 50 ks).

The colliding galaxies NGC 2207/IC 2163 are estimated to be at a distance of $39.6 \pm 5.5 \text{ Mpc}$ (Arnett 1982), which is based on measurements of type Ia SNe (see NASA/IPAC Extragalactic Database ‘NED’). Fig-

⁸ However, recent evidence has been reported (Harrison et al. 2014, in prep.) that at least one ULX (in M 82) may in fact be an accreting neutron star.

ure 1 shows a collection of images of NGC 2207/IC 2163 recorded with the Hubble Space Telescope (*HST*), *GALEX*, *Spitzer*, and *Herschel*, all to the same scale and orientation. The larger (smaller) galaxy on the right (left) is NGC 2207 (IC 2163). The collisional dynamics of such galaxy pairs in general, and of NGC 2207/IC 2163 in particular, have been well modeled with N-body codes (see, e.g., Struck et al. 2005, and references therein). Such simulations can, for example, indicate which of the currently observed features in these galaxies have been created or substantially modified by the collision. The consensus is that the major spiral arms of NGC 2207 existed prior to the collision, and have not been substantially perturbed by the interaction. By contrast, the noteworthy “ocular” feature in IC 2163 (see, in particular, the *Spitzer* 8- μ m image) was apparently produced in the encounter. These facts indicate that the collision between NGC 2207 and IC 2163 is likely in its initial phases, e.g., for perhaps only a single orbit of the galaxy pair. Given the timescale for this grazing encounter, the star formation that has been induced has likely been underway only for the past dynamical timescale, i.e., a few times 10^8 yr. Mass estimates for NGC 2207 and IC 2163 (including dark matter), used in the Struck et al. (2005) simulations as well as those measured by Mineo et al. (2013), are quite comparable at 1.5×10^{11} and $1.1 \times 10^{11} M_{\odot}$, respectively, for the two galaxies.

In the present paper we reinvestigate the X-ray emission from this same galaxy pair with about five times the net *Chandra* exposure (63 ks vs. 13 ks) used for our previous study. NGC 2207/IC 2163 was observed with *Chandra* on three subsequent occasions for a total additional exposure of 50 ks. This deeper exposure enables more sensitive studies of the X-ray population (3.4×10^{38} erg s $^{-1}$ vs 10^{39} erg s $^{-1}$) and diffuse emission. The four different epochs also allow us to study the long-term variability of individual sources and that of the XLF. We also utilize multiwavelength data from the *GALEX*, *Spitzer*, *Herschel*, and Two Micron All Sky Survey (2MASS) archives. In Sect. 2 we describe the data products and the basic steps in the analysis. We discuss the 56 point sources (excluding the central AGN) detected in the combined exposures, including 28 ULXs, in Sect. 3. In this same section we present cumulative luminosity functions for the individual exposures as well as for the sum; we discuss the X-ray source variability; and we search for optical and infrared counterparts to the X-ray sources. In Sect. 4 we describe the construction of spatially-resolved maps of SFR density and $L_{\text{IR}}/L_{\text{NUV}}$, along with the related multiwavelength data acquisition. In Sect. 5 we repeat our correlation study between the *local* star formation rate in NGC 2207/IC 2163 and the number and X-ray luminosity of the ULXs – this time with improved significance. As a new feature of the analysis, in Sect. 6 we also compute the correlation between a *local* $L_{\text{IR}}/L_{\text{NUV}}$ and the number and luminosity of the ULXs, with quantitative considerations about the age of the stellar population associated with bright X-ray binaries. The spectrum of the diffuse emission is presented in Sect. 7. Summary and Conclusions follow in Sect. 8.

2. X-RAY ANALYSIS

2.1. Data preparation

We analyzed four *Chandra* ACIS-S observations of the galaxy pair NGC 2207/IC 2163 (see Table 1). The data reduction was done following the standard CIAO⁹ threads (CIAO version 4.6, CALDB version 4.5.9) for soft (0.5–2 keV), hard (2–8 keV) and broad (0.5–8.0 keV) energy bands. All *Chandra* datasets were reprocessed using `chandra_repro`, a script that automates the recommended data processing steps presented in the CIAO analysis threads. Using the script `fluximage` we computed a monochromatic exposure map for the mean photon energy of each band: 1.25 keV, 5.0 keV and 4.25 keV for the soft, hard and broad band respectively. `fluximage` outputs both the instrument map for the center of each energy band using the tool `mkinstmap`, and the exposure maps in sky coordinates for each energy band using `mkexppmap`.

The four observations were also combined in order to improve the sensitivity. Prior to merging, we first corrected the individual aspect solution, using `wcs_update`. In particular, we modified the right ascension (α), the declination (δ) and roll angle to match those of the observation with the longest exposure time (Obs. ID 14914, see Table 1). To do so, we ran CIAO `wavdetect` on each observation and used the output coordinates of one point source which is persistent and present in all 4 observations, $\alpha = 94.071833$, $\delta = -21.380642$, as a common fiducial point. We did not choose the central AGN of NGC 2207 for that purpose, because `wcs_update` uses the centroid of the chosen point source and the central AGN has a non-symmetric shape. The new aspect solution was then used to reproject all the original event files into the sky coordinates of Obs. ID 14914, using `reproject_events`. The new event files and aspect solutions were then merged using `reproject_obs` and the individual and combined images, exposure maps, exposure-corrected images were created using `flux_obs`.

The detection of point sources was carried out in the 0.5–8 keV band on all individual reprojected observations as well as on the combined observation, using CIAO `wavdetect`. To account for the variation of the *Chandra* point spread function (PSF) effective width from the inner to the outer parts of the CCD chip, we used the $\sqrt{2}$ -series from 1.0 to 8.0 as the scale parameter. The value of the `sighthresh` parameter was set as the inverse of the total number of pixels in the image ($\sim 10^{-6}$, $D25$ area only) in order to avoid false detections. We used `maxiter` = 10, `iterstop` = 0.00001 and `bkg sighthresh` = 0.0001. The `wavdetect` parameter `psffile` was set differently for individual and combined observations. For single observations we used the tool `mkpsfmap` to compute a PSF map that carries information about the PSF-size for each pixel in the input image at 1.5 keV for an 80% enclosed counts fraction. However, `mkpsfmap` cannot be used on the combined image. In this case we created an exposure-map-weighted PSF map using `dmimgcalc`. This is the best approach when the roll angles of individual observations differ¹⁰, which is the case for our data.

2.2. Source photometry

⁹ <http://cxc.harvard.edu/ciao4.6/index.html>

¹⁰ http://cxc.harvard.edu/ciao/threads/wavdetect_merged/

TABLE 1
NGC2207/IC2163 *Chandra* OBSERVATION LOG.

Obs.ID	Obs.Start	Exp.Time	Obs.Mode	Camera
(1)	(UT) (2)	(ks) (3)	(4)	(5)
11228	2010-07-18 11:04:33	12.88	VF	ACIS-S
14914	2012-12-30 04:22:44	19.85	F	ACIS-S
14799	2013-04-07 21:49:16	9.84	VF	ACIS-S
14915	2013-08-24 04:20:31	19.84	F	ACIS-S

NOTE. — (1) *Chandra* identification numbers, (2) Start date and time of the observation, (3) Exposure Time in kilo-seconds, (4) Observing mode (F: faint mode; VF: very faint mode), (5) Observing instrument.

The aperture-corrected X-ray photometry of compact sources was performed using the same approach and scripts as in our first paper on NGC 2207/IC 2163 (see Mineo et al. 2013, and references therein). Briefly, the count rate for each detected point source was calculated inside a circular region centered on the source coordinates given by the *wavdetect* output. In order to determine the radius of the circle, for each observation we extracted the PSF using CIAO 4.4 *mkpsf* task. For the merged observation, the PSFs in single images were combined using the values of the exposure maps as weights. The PSFs were mapped into the World Coordinate System (WCS) reference frame of the relative point source image using *reproject_image* task. The radius of the circle was determined individually for each source so that the encircled PSF energy was 90%. The background region was defined as an annulus with inner radius equal to the radius of the source region and outer radius 3 times larger. For a detailed description of the procedure and its caveats we refer to Section 3.2 in Mineo et al. (2012a).

A number of compact sources were found to have background regions overlapping their neighboring sources. In these cases we excluded the 90% PSF circular regions of the overlapping point sources from the image in order to subtract the source contribution from the background counts; these regions were also subtracted from the exposure map to correct the source area. The procedure for the aperture-corrected photometry described above was then repeated using the corrected image and exposure map.

2.3. Luminosities and hardness ratios

The net count rates measured in the 0.5–8.0 keV band for each X-ray point source (Sect. 2.2) were converted into fluxes, i.e., units of $\text{erg cm}^{-2} \text{s}^{-1}$. The count-rate-to-flux conversion factor was obtained as follows. For each observation, we first extracted the *combined* spectrum of all point sources detected within the *D25* ellipse that have a number of net counts ≥ 10 , in order to avoid undue contamination from diffuse emission and faint unresolved X-ray sources¹¹. The task *dmextract* was used for this purpose and the central source was excluded from the multi-source region, as it may be an active galactic

¹¹ At this stage we only have the count rates for each X-ray point source, not yet their luminosities. We note that after having obtained the source luminosities (Sect. 2.3) and after having performed the completeness analysis (Sect. 2.4), the selection of sources with net counts ≥ 10 corresponds to an average of $\sim 90\%$ of the sources detected above the completeness luminosity in each observation (Table 2).

nucleus (AGN) (Elmegreen et al. 2006; Kaufman et al. 2012). Using the *sky2tdet* tool we obtained the weights maps that are needed to create the weighted Ancillary Response Files (ARF) with *mkwarf*. The weighted Response Matrix Files (RMF) were created using *mkrmf*. The background spectrum was similarly extracted from multiple large regions between, and far enough from, the point sources, within the *D25* ellipse, on the same detector chip. Finally, we used the script *combine_spectra* to sum the four composite source spectra, associated background spectra and source and background ARF and RMF instrument responses.

The final spectrum was binned in order to have a minimum of 20 counts per channel to apply χ^2 statistics. This background-subtracted co-added spectrum (see Sect. 7) was modeled as an absorbed power law using XSPEC v. 12.7.1b. The best-fit parameters for this model are $N_{\text{H}} = (3.0 \pm 0.3) \times 10^{21} \text{ cm}^{-2}$ and $\Gamma = 1.95 \pm 0.08$, with $\chi^2 = 78.4$ for 76 degrees of freedom (i.e., reduced $\chi^2 = 1.03$). This is in full agreement with the results of the population study by Swartz et al. (2004), who showed that the distribution of the power-law photon indexes for luminous compact X-ray sources in star-forming galaxies is centered on $\Gamma = 1.97 \pm 0.11$.

Our best-fit absorbed power law was adopted to convert the net count rate of each detected point source into a flux ($\text{erg cm}^{-2} \text{s}^{-1}$). The fluxes were then converted into luminosities (erg s^{-1}) assuming a distance of 39.6 Mpc (Arnett 1982).

Since we do not have sufficient statistics for X-ray spectral fitting of individual sources, to investigate the ULX spectral properties we used hardness ratios. The procedure described in Sect. 2.2 was applied to the reference source list to obtain count rates in both soft (*S*: 0.5–2 keV) and hard (*H*: 2–8 keV) bands. The respective source counts were used to calculate the X-ray hardness ratio as:

$$\text{HR} = \frac{H - S}{H + S} \quad (1)$$

2.4. Completeness analysis

Following the method and tools of Voss & Gilfanov (2006), we computed the completeness function $K(L_{\text{X}})$ for all individual *Chandra* observations, as well as for the combined one, within the *D25* region. We define the “completeness luminosity” L_{C} , as the luminosity at which $> 90\%$ of point sources are detected in the 0.5–8 keV band, corresponding to $K(L_{\text{C}}) = 0.9$ (i.e., no more than 10% of the sources within the *D25* are missing). The values of L_{C} at the assumed distance of 39.6 Mpc for each observation are listed in Table 2.

3. LUMINOUS X-RAY SOURCES

3.1. Discrete source content

In Table 2 we list the number of compact sources detected with luminosities above L_{C} within the *D25* region, with significance of at least 3σ , along with their integrated luminosity. The same table also includes the expected number and luminosity of background AGN computed above an equivalent L_{C} within the *D25* region. The contribution of background AGNs was estimated using the $\log N - \log S$ function of Georgakakis

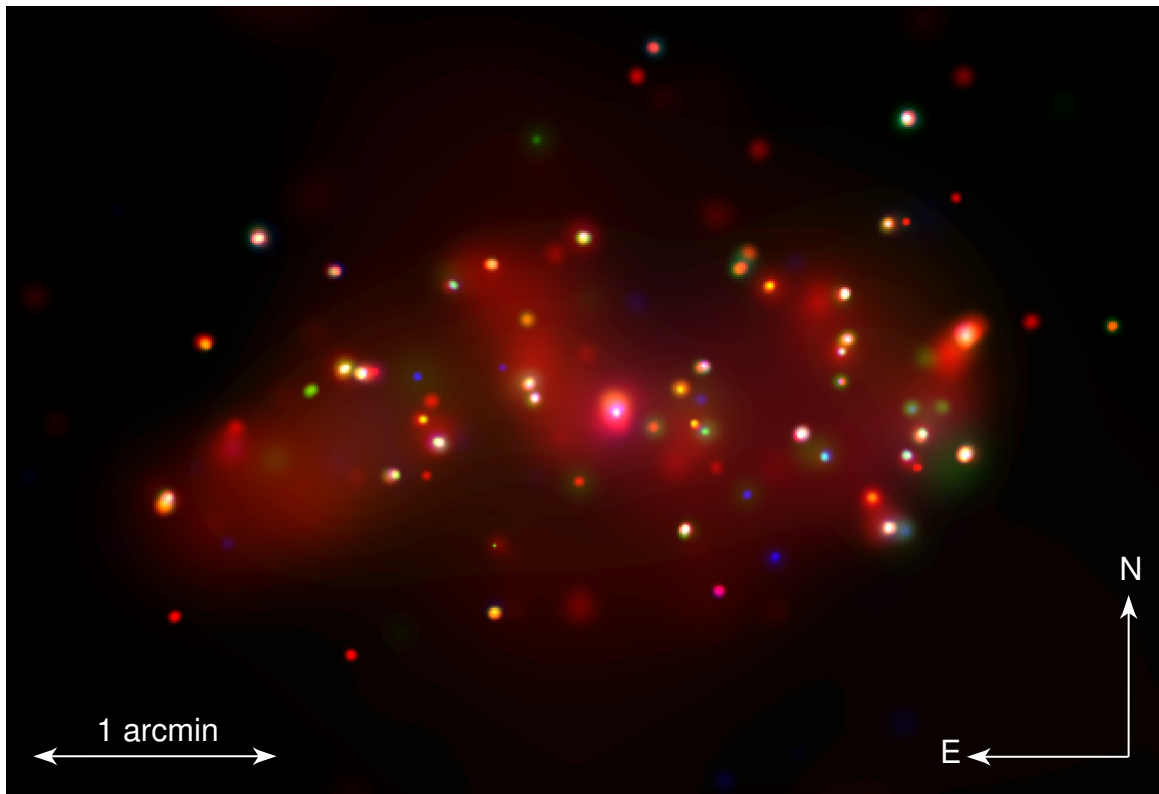


FIG. 2.— *Chandra* X-ray image of the colliding galaxies NGC 2207 and IC 2163. Red corresponds to soft (0.2–1.5 keV), green to medium (1.5–2.5 keV), and blue to hard (2.5–8.0 keV) X-ray photons. We note that the definition of “soft” and “hard” photons used to generate this figure is different than that utilized in the data analysis and calculation of hardness ratio. A soft diffuse X-ray component is quite prominent in the image. This image was adaptively smoothed using the CIAO task `csmooth` (with the minimum signal-to-noise set to 2).

et al. (2008). We converted their $\log N - \log S$ function defined over the 0.5–10 keV band, to apply in our somewhat more narrow band (0.5–8 keV). After obtaining the predicted total flux of background AGNs, S_{AGN} , above the completeness threshold flux, S_C , we computed the equivalent AGN luminosities as $4\pi D^2 S_{\text{AGN}}(> S_C)$, where D is the distance to the galaxy pair. From Table 2 it is evident that the contribution of background AGNs to the bright X-ray compact source population of NGC 2207/IC 2163 is within the 5–7% range.

The properties of the X-ray point sources detected within the $D25$ ellipse are listed in Tables A1, A2, A3, A4 and A5. For all sources in each observation, we provide the *Chandra* positions, the net counts after background subtraction in several bands, the hardness ratio, the X-ray luminosity, and the X-ray flux. There were 74 sources detected in the composite image, 57 of which ($\sim 77\%$) were above the completeness luminosity. One source in each observation is associated with the low-luminosity AGN near the center of NGC 2207 (Kaufman et al. 2012) and is indicated with a † symbol in the Tables in the Appendix.

We indicate, with a ‡ symbol, the X-ray source associated with the elongated soft X-ray feature, called *feature i* by Elmegreen et al. (2000). This source has a spectrum compatible with the rest of ULXs (see Fig. 4) and could actually be a ULX embedded in the diffuse emission. Smith et al. (2014) also found that this source is quite extended, but with a low surface brightness, and that it has a soft X-ray spectrum as well as a similar

X-ray flux to that measured in the present work.

The feature is located in the outer spiral arm of NGC 2207, $\sim 1.5'$ N-W from its center in the middle of a dusty starburst region. Other symbols (\star , \diamond and \ast) are used to indicate X-ray sources that match (within $\sim 3''$) the position of the supernovae (SNe) hosted by NGC 2207: SN 2003H, SN 2013ai, SN 1999ec.

A *Chandra* X-ray image of NGC 2207/IC 2163 is shown in Fig. 2. It was obtained by combining the four available observations (see Table 1) and it unveils the presence of soft diffuse emission (discussed in Sect. 7) in addition to the bright X-ray compact source population. The signal from diffuse emission is weak and was apparently not visible in the single pointing (Obs. ID 11228) analyzed in our previous paper (Mineo et al. 2013). The detection of diffuse emission in the current work is also aided by the fact that we now use the CIAO task `csmooth`, while in the previous paper only a Gaussian smoothing kernel was applied.

In Fig. 3 we show the locations of the 57 point X-ray sources above the completeness threshold superposed on the *HST* image of NCC 2207/IC 2163. Not surprisingly, many of these sources lie along the prominent spiral arms of NGC 2207 (larger galaxy on the right), though the same does not seem to follow for the smaller galaxy IC 2163.

In Fig. 4 the net photon fluxes (photons $\text{cm}^{-2} \text{s}^{-1}$) in the 0.5–8 keV band are plotted versus the hardness ratios defined in Eq. (1), for all point sources detected above the completeness luminosity of each individual observa-

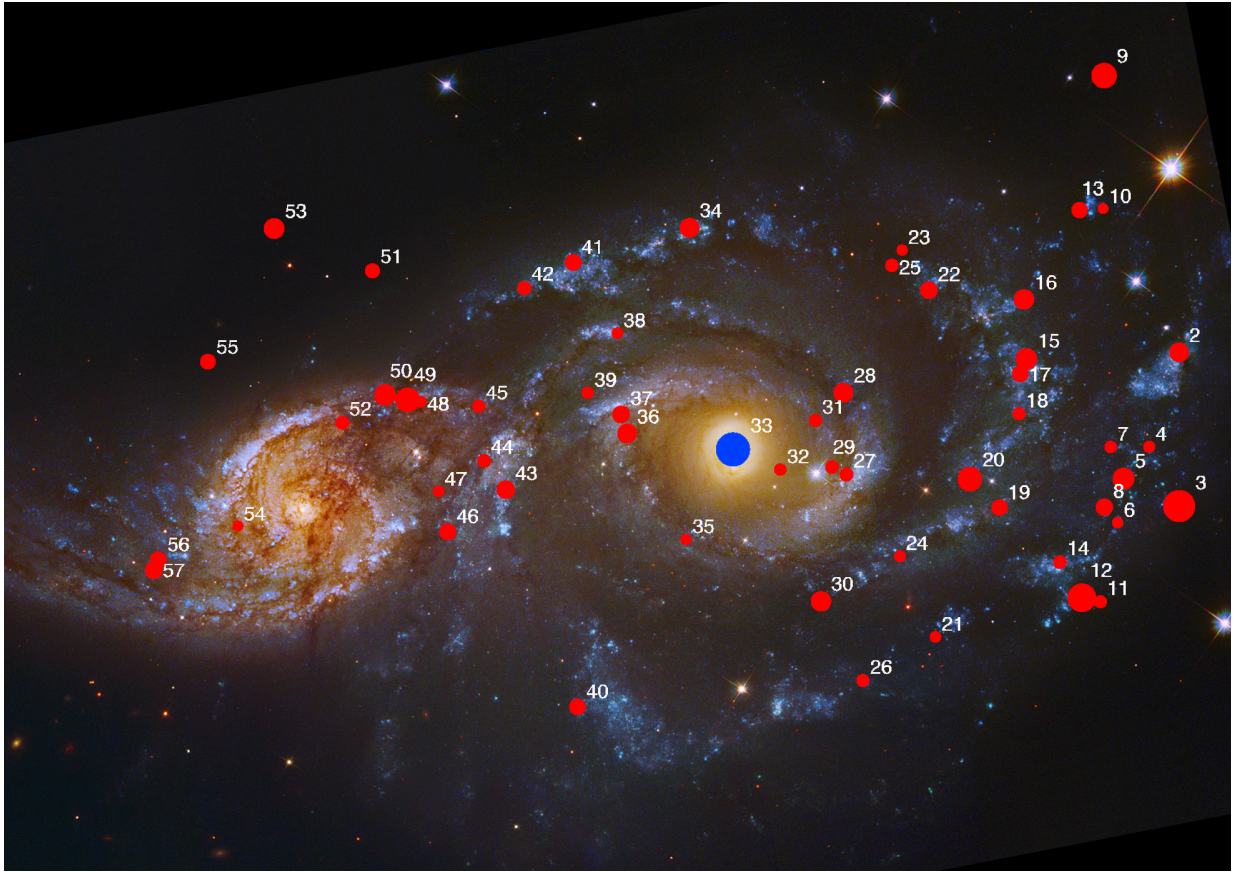


FIG. 3.— HST image of the galaxy pair NGC 2207/IC 2163 (WFPC2 camera using filters F336W, F439W, F555W and F814W Elmegreen et al. 2000). The superposed filled red circles mark the locations of the 56 point X-ray sources detected in the four combined *Chandra* observations above the completeness limit ($3.4 \times 10^{38} \text{ erg s}^{-1}$; Table 2). The size of each circle is proportional to the cube root of the luminosity of the X-ray source.

tion (see Table 2 for details). The sources are indicated with four different colors, depending on the observation in which they were detected. The figure shows that the bulk of ULXs in NGC 2207/IC 2163 have a soft spectrum ($HR < 0$). The hardness ratios measured for the central AGN are well separated from the ULX population, having a harder ($0.5 < HR < 1$) spectrum and being bright.

We also note that the spectrum of the X-ray source matching the position of the supernova SN 2013ai, detected in Obs.ID 14799, is harder than the spectrum of the bulk of the ULXs. Most type II SNe have X-ray spectra well described by a $kT = 1 \text{ keV}$ to $kT = 10 \text{ keV}$ mekal model, but a couple type II_{in} SNe have been observed with rather hard X-ray spectra, e.g., a power law with photon index of -0.2 in SN 2005kd (Pooley et al. 2007) and a power law with photon index of 1.1 in SN 2001em (Pooley & Lewin 2004).

3.2. X-ray luminosity function

After excluding the central AGN, we constructed the cumulative X-ray luminosity function (XLF) of the X-ray point sources in NGC 2207/IC 2163, for each individual observation and for the combined observations (left and middle panels of Fig. 5). The cumulative luminosity distribution of background AGNs (see Sect. 3.1 for details) is marked in the middle panel of Fig. 5 by a dot-dashed (grey) curve. Fig. 5 shows that combining the four *Chandra*

observations allowed for a significant improvement in sensitivity: $3.4 \times 10^{38} \text{ erg s}^{-1}$ vs $\sim 10^{39} \text{ erg s}^{-1}$ for the individual observations (see also column 2 in Table 2).

The XLF was modeled with a simple power law. We fixed the cut-off at $L_{\text{cut}} = 10^{41} \text{ erg s}^{-1}$, i.e., a luminosity exceeding that of the brightest detected compact source ($L_{0.5-8 \text{ keV}} = 1.2 \times 10^{40} \text{ erg s}^{-1}$, detected in Obs.ID 11228):

$$N(> L_{38}) = \xi \times L_{38}^{-\gamma}, \quad L \leq 10^{41} \text{ erg s}^{-1}. \quad (2)$$

We fitted the cumulative XLFs using a Maximum Likelihood (ML) method. The best-fitting power law slopes for individual observations are listed in column (7) of Table 2. They range between 1.04 and 1.56 (corresponding to 2.04 and 2.56 in differential form). The ML fit of the combined observations yielded a slope of $\gamma = 0.92^{+0.14}_{-0.13}$, (1.92 in differential form) which is indicated with a green line on the middle panel of Fig. 5. This slope is steeper than the typical slope of ≈ 0.6 (1.58 ± 0.02 in differential form) found for the high-mass X-ray binary (HMXB) luminosity distributions below $\sim 10^{40} \text{ erg s}^{-1}$ (Grimm et al. 2003; Swartz et al. 2011; Mineo et al. 2012a). In our previous work, (Mineo et al. 2013), we found a similar result and speculated that this might have been related to the limited sensitivity of the single *Chandra* observation (Obs. ID 11228) that we analyzed. In fact, with a sensi-

TABLE 2
COMPLETENESS LUMINOSITIES AND GLOBAL SOURCE PROPERTIES.

Obs. ID	L_C (erg/s)	$N_X(> L_C)$	$L_X(> L_C)$ (erg/s)	$N_{AGN}(> L_C)$	$L_{AGN}(> L_C)$ (erg/s)	XLF slope γ
(1)	(2)	(3)	(4)	(5)	(6)	(7)
11228	1.2×10^{39}	20	6.4×10^{40}	1.4	7.0×10^{39}	$1.32^{+0.33}_{-0.29}$
14914	8.2×10^{38}	27	7.1×10^{40}	1.9	7.5×10^{39}	$1.04^{+0.23}_{-0.21}$
14799	1.3×10^{39}	23	6.9×10^{40}	1.3	6.9×10^{39}	$1.56^{+0.36}_{-0.31}$
14915	7.7×10^{38}	26	5.2×10^{40}	2.0	7.6×10^{39}	$1.27^{+0.27}_{-0.24}$
Combined	3.4×10^{38}	56	7.8×10^{40}	3.6	8.4×10^{39}	$\dagger 0.92^{+0.14}_{-0.13}$

NOTE. — All values are referred to the $D25$ ellipse of NGC2207/IC2163. (1) *Chandra* identification numbers; (2) completeness luminosity at which $> 90\%$ of point sources are detected in the 0.5–8 keV band; (3) number of point sources detected above L_C (the central AGN was excluded from this number); (4) cumulative 0.5–8 keV luminosity of compact sources above L_C ; (5) expected number of background AGNs above the completeness luminosity; (6) expected equivalent luminosity of the background AGNs. See Sect. 2.4 for details; (7) best-fitting XLF slope of the simple power-law model (eq. 2), in cumulative form. \dagger We fitted the combined XLF with a power law model with an exponential cut-off (eq 3), obtaining a best-fitting slope $\alpha = 0.66 \pm 0.04$ (1.66 in differential form) and the exponential cut-off at $L_o = (3.39 \pm 0.28) \times 10^{39} \text{ erg s}^{-1}$ (see Section 3.2 for details).

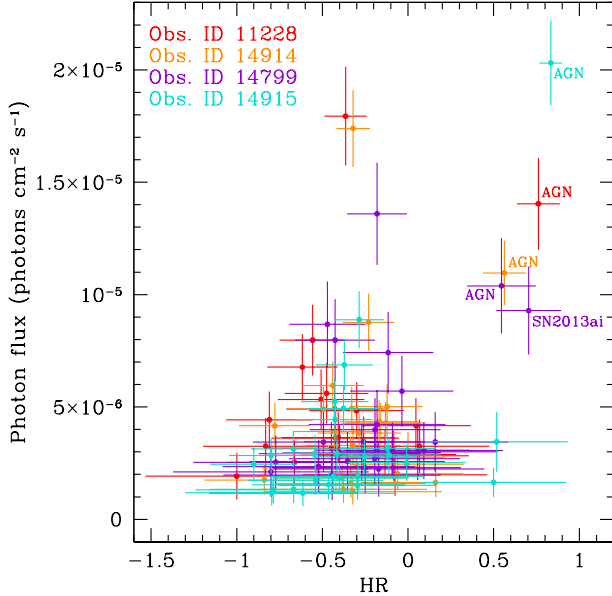


FIG. 4.— Net photon fluxes in 0.5–8 keV band versus hardness ratios (HR, Eq. (1)), for all point sources detected above the completeness luminosity of each individual observation (see Table 2 for details). The sources are indicated with four different colors, depending on the observation where they were detected. The central AGN is well separated from the ULX population, having a harder ($0.5 < \text{HR} < 1$) spectrum and being bright. We also note that the spectrum of the supernova SN 2013ai, detected in Obs.ID 14799, is harder than that of the bulk of ULXs.

tivity of $\sim 10^{39} \text{ erg s}^{-1}$, we could be observing only the high-luminosity roll-off of the power-law distribution that extends to lower luminosities with a slope similar to 1.6. In the present work we improved the sensitivity down to $3.4 \times 10^{38} \text{ erg s}^{-1}$ by combining four observations. We also fitted the combined XLF using a power law model with an exponential cut-off:

$$N(> L_{38}) = \xi \times L_{38}^{-\alpha} \exp(-L_{38}/L_o), \quad (3)$$

which yielded a best-fitting slope $\alpha = 0.66 \pm 0.04$ (1.66

in differential form) and the exponential cut-off at $L_o = (3.39 \pm 0.28) \times 10^{39} \text{ erg s}^{-1}$. The slope is now in full agreement with that of the average XLF for HMXBs, and the exponential cut-off somewhat confirms the speculation that we may be observing only the bright end roll-off of a more extended power law distribution with slope 1.6.

We performed a Kolmogorov-Smirnov (KS) test to determine the goodness of fit. The test statistic D_{KS} , i.e., maximum absolute value of the differences between the two distributions, is 0.31 and 0.27 for the power-law and exponentially cut-off power-law models respectively. The p -values for the two-sided hypothesis are 5.5×10^{-4} and 3.8×10^{-3} respectively, i.e. smaller than the canonically assumed significance level of 0.05 for rejection. Formally the null hypothesis is rejected, but it still appears to be a good qualitative fit.

The observed power law roll-off is due to the lack of sources brighter than $\sim 10^{40} \text{ erg s}^{-1}$, also observed in our previous work (Mineo et al. 2013). However, this could well be expected based on the star formation rate (SFR) of NGC 2207/IC 2163: the number predicted by the XLF from Mineo et al. (2012a) for bright HMXBs is marginally consistent (2 ± 1.4) with what we observe.

3.3. ULX variability

To investigate the variability of the ULX population of the colliding galaxy pair NGC 2207/IC 2163, we started from the list of sources detected in the combined observation. At the position of each detection, we used the same tools and technique as described in Sect. 2.2 to measure the net number of counts and the net photon flux (photons $\text{cm}^{-2} \text{ s}^{-1}$) in each individual observation, in the soft (0.5–2 keV), hard (2–8 keV) and full (0.5–8 keV) bands. The soft and hard source counts were used to calculate the X-ray hardness ratios as in Eq. (1). The full band count rates were used to investigate the source variability, following Fridriksson et al. (2008), by means of the significance S_{flux} for long-term flux variability:

$$S_{\text{flux}} = \max_{i,j} \frac{|F_i - F_j|}{\sqrt{\sigma_{F_i}^2 + \sigma_{F_j}^2}}, \quad (4)$$

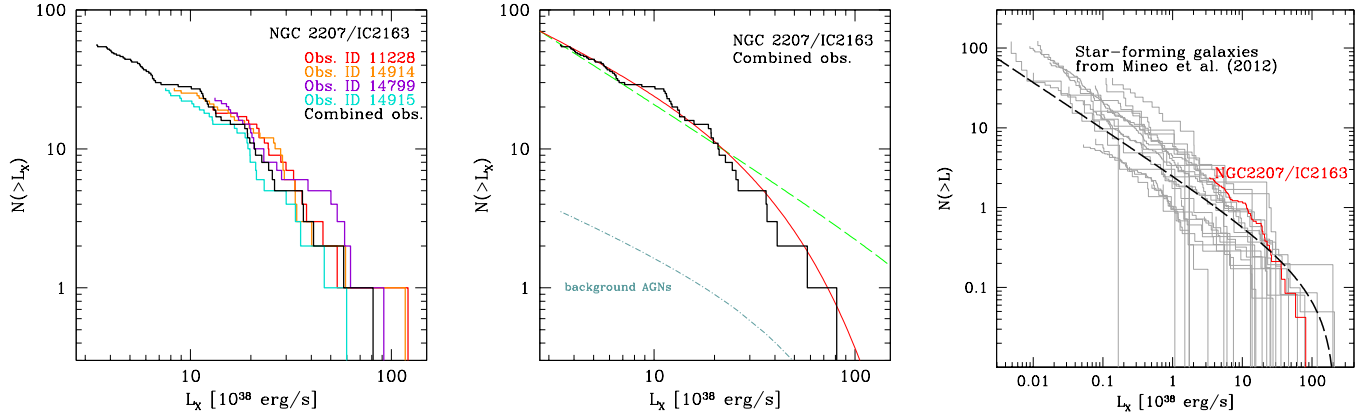


FIG. 5.— (Left) Cumulative X-ray luminosity distributions of the compact sources detected within the $D25$ ellipse, above the completeness luminosity of the galaxy pair NGC 2207/IC 2163: Obs. ID 11228 (red), Obs. ID 14914 (orange), Obs. ID 14799 (purple), Obs. ID 14915 (cyan), combined observations (black). The central AGN is not included. (Center) Cumulative X-ray luminosity function of the combined observations (black), along with its best-fitting models: simple power-law (Eq. 2) with $\gamma = 0.92^{+0.14}_{-0.13}$ (dashed green) and power-law model with $\alpha = 0.66 \pm 0.04$ and exponential cut-off at $L_o = (3.39 \pm 0.28) \times 10^{39} \text{ erg s}^{-1}$ (solid red, Eq. 3). The grey, dot-dashed curve shows the predicted level of resolved background AGNs, relative to the combined XLF and based on results from Georgakakis et al. (2008). (Right) The cumulative XLF of NGC 2207/IC 2163 (red) from the combined observations, normalized by its SFR ($23.7 M_{\odot} \text{ yr}^{-1}$, Mineo et al. (2013, Table 2)), plotted along with the cumulative XLFs of individual star-forming galaxies from Mineo et al. (2012a) (grey), normalized by their respective SFRs. The dashed black line is the average cumulative XLF per unit SFR, given by integration of their equation (18).

where: F_i , F_j are the net photon fluxes in the i^{th} and j^{th} *Chandra* observations, and σ_{F_i} , σ_{F_j} are the respective uncertainties. A source is *variable* if $S_{\text{flux}} > 3$, and it is a *transient* candidate if it is variable ($S_{\text{flux}} > 3$) and its measured flux is consistent with zero during at least one observation. For sources with zero counts (therefore null count rate $F_{i,j} = 0$) we used the 1σ upper limit for zero counts assuming Poisson statistics, based on the tables in Gehrels (1986), which is 1.84 counts. We converted to photon flux uncertainty $\sigma_{F_{i,j}}$ by dividing the 1σ upper limit for zero counts by the value of the exposure map ($\text{cm}^2 \text{ s counts photon}^{-1}$) at the position of the source.

In total, 12 sources out of 57 ($\sim 20\%$ including the AGN at the center of NGC 2207) show significant long-term variability ($S_{\text{flux}} > 3$). Of these, 7 are transient candidates (sources No. 51, 31, 37, 74, 22, 46, 66). We list all the variable sources and transient candidates in Table 6, along with their count rates in the 0.5–8 keV band, the hardness ratios (computed with Eq. 1) and the significance, S_{flux} , of the variability. The long term light curves of these sources are shown in Fig. 6. The ratio between maximum and minimum count rate ranges between 2 and 3.8 for variable sources, and between ~ 34 and ~ 72 for transient candidates. One of the variable sources (#41 in Table 6) is the central AGN in NGC 2207. Another one (#22 in Table 6), is associated ($0.11''$ separation) with the supernova SN 2013ai. The source was detected only during Obs. ID 14799, where it happens to have a rather hard X-ray spectrum ($\text{HR} \sim 0.7 \pm 0.2$) and 0.5–8 keV luminosity $L_X = (6.3 \pm 1.3) \times 10^{39} \text{ erg s}^{-1}$ (see Table A3).

Correlated X-ray spectral and luminosity changes have been observed in a number of ULXs (e.g., Kubota et al. 2001; Pintore et al. 2014). Fig. 4 shows no significant long term variability in the hardness ratio of the ULXs

in NGC 2207/IC 2163. It also shows that there are no other sources located close to the AGN in the $\text{HR} > 0.5$ area of the diagram, suggesting there are probably not many background AGN among the sources shown here, in line with our other estimates (see Sect. 3.1).

We looked more carefully for possible spectral changes in the 12 variable sources mentioned above, and found none. The lack of such changes is common when the flux variability is only a factor of a few (Fridriksson et al. 2008; Soria et al. 2009; Webb et al. 2014).

3.4. *HST* and *Spitzer* counterparts

Using *HST* images of NGC 2207/IC 2163, Elmegreen et al. (2001) identified 17 optical “super-star clusters” (SSC, mass $1\text{--}20 \times 10^4 M_{\odot}$) within the galaxy pair, with $M_V \leq -10.3$. We cross checked the coordinates of the SSCs (D. Elmegreen & M. Kaufman, private communication) with the coordinates of the 74 X-ray sources detected within the $D25$ ellipse in the co-added *Chandra* image (Table A5). We found that only one source is coincident, within a $1.5''$ tolerance limit, with an SSC. Our source #48, $L_X = (4.1 \pm 1.5) \times 10^{38} \text{ erg s}^{-1}$, is a very close match ($0.13''$) to the SSC #16 in Elmegreen et al. (2001), which has the following colors and magnitude: $M_V = -11.5$, $U - B = -1.6$, $B - V = -0.7$, $V - I = 0.5$. The $V - I$ color is compatible with a young or an intermediate age SSC (Elmegreen et al. 2001, and references therein). However, the B-V color is much bluer than is typical for either a young or intermediate SSC (Elmegreen et al. 2001, and references therein), and is therefore indicative of a younger population. Similarly, Voss et al. (2011) found two ULXs coincident with young massive stellar clusters in M 82 and NGC 7479 (M82 X-1 and CXOU J230453.0+121959 respectively). They concluded that rarity of observing ULXs inside massive clusters makes it unlikely that most ULXs are formed

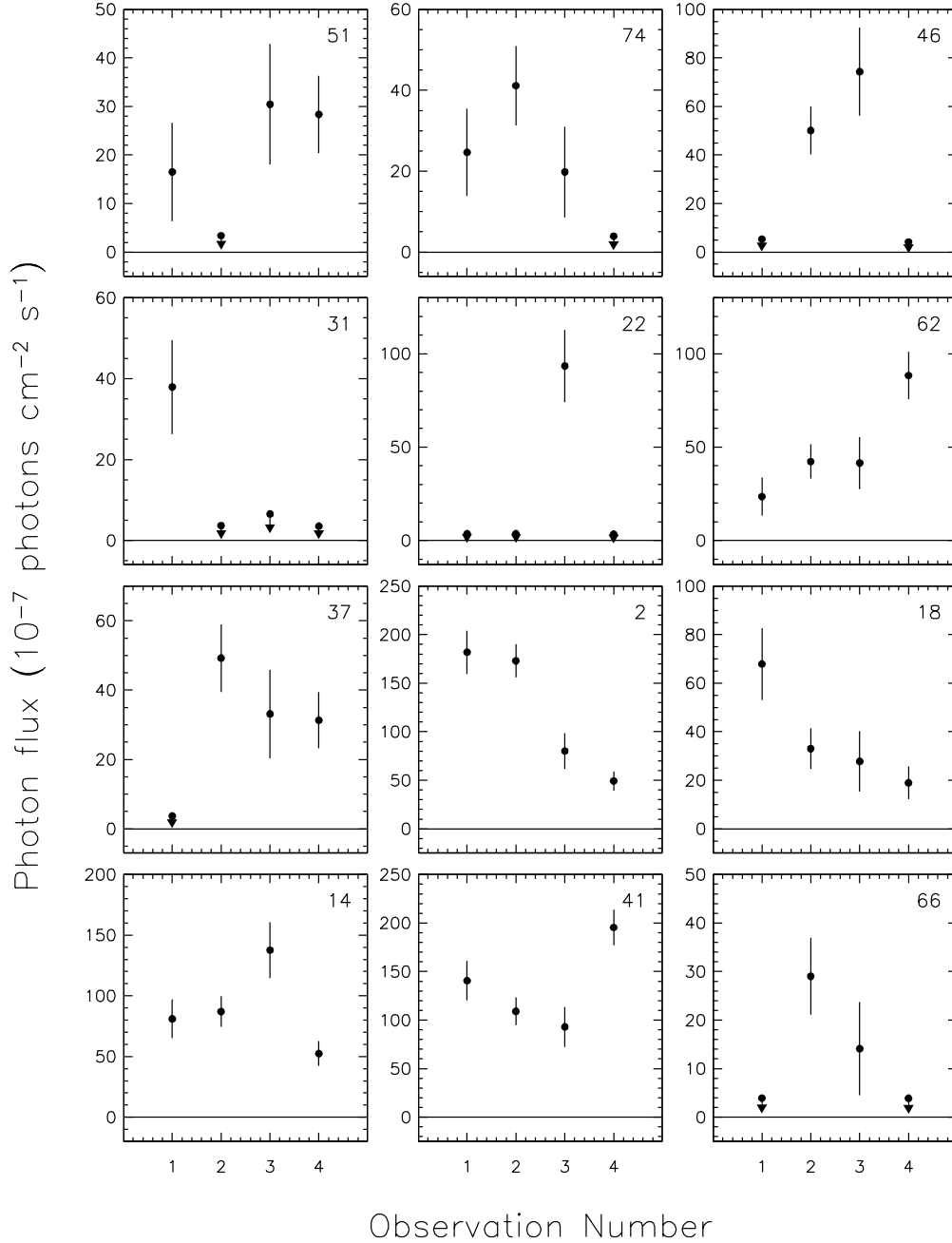


FIG. 6.— Long-term *Chandra* light curves of the 12 sources with significant variability listed in Table 6. The observation numbers on the x-axis correspond to the four individual observations: 1: Obs. ID 11228 (2010-07-18), 2: Obs. ID 14914 (2012-12-30), 3: Obs. ID 14799 (2013-04-07), 4: Obs. ID 14915 (2013-08-31). The flux on the y-axis is in units of 10^{-7} photons $\text{cm}^{-2} \text{s}^{-1}$ and it was measured as described in Sections 2.2 and 3.3. Sources #51, 31, 37, 74, 22, 46 and 66 are ULX transient candidates. Source 22 is associated (0.11'' separation) with the supernova SN 2013ai. Source 41 is the central AGN in NGC 2207. Source numbers are based on Table A5.

inside clusters, unless they are kicked out of the clusters at birth.

The 74 X-ray sources in Table A5 were also cross-correlated with the positions of the 225 *Spitzer* 8-micron clumps identified by Elmegreen et al. (2006). We found a statistically significant set of $\sim 1/3$ of our X-ray sources which align with *Spitzer* 8-micron clumps, and half of the matching sources are ULXs. Among the matches there are two SNe (SN 1999ec and SN 2013ai), as well as the

extended X-ray source at the location of the dusty star-burst region called “*feature i*” (Elmegreen et al. 2000). Since the young star-forming regions represented by the IR clumps are unresolved below ~ 370 pc (due to the *Spitzer* angular resolution at $8 \mu\text{m}$), and this is much larger than individual OB associations, it is possible that these star complexes may also include some older stars (Kaufman et al. 2012).

Overall, we found almost no interesting correlation be-

tween the bright X-ray sources and the *HST*-detected SSCs, and we conclude that the SSCs in this galaxy pair don't typically host luminous X-ray sources. On the contrary, $\sim 1/3$ of the X-ray sources detected in our co-added *Chandra* observation match up with the $8\,\mu\text{m}$ -detected young star complexes.

As an added note, we report that our X-ray source #18 corresponds to source "X1" in Kaufman et al. (2012), centered on a collection of blue star clusters, the most prominent of which lies close to a discrete radio source. Based only on one *XMM-Newton* observation, the latter authors interpreted their source X1 as a possible radio SN, a SNR, or a background quasar. We believe that our X-ray source #18 is a ULX for two reasons. First, the source shows significant variability (see Fig. 6). It has been detected in all four *Chandra* pointings, with a peak luminosity of $L_X = (4.6 \pm 1.0) \times 10^{39} \text{ erg s}^{-1}$ in Obs. ID 11228, and decreasing down to $L_X = (1.3 \pm 0.5) \times 10^{39} \text{ erg s}^{-1}$ by Obs. ID 14915. Second, the source is soft during all four observations, with a spectral hardness ranging between -0.32 ± 0.28 and -0.62 ± 0.21 and, therefore, is incompatible with an AGN that typically have harder spectra (see, e.g. Sazonov et al. 2008, as well as Fig. 4 this work).

4. SPATIALLY-RESOLVED MAPS OF SFR DENSITY AND EXTINCTION

Using only the data from *Chandra* Obs. ID 11228, along with *Spitzer* $24\,\mu\text{m}$ and *GALEX* FUV images, Mineo et al. (2013) investigated, for the first time, the spatial and luminosity distributions of ULXs as a function of the local SFRs within a galaxy. They found that the relation between the total number of ULXs and the integrated SFR of the host galaxy (Mapelli et al. 2010; Mineo et al. 2012a; Smith et al. 2012) is also valid on *sub-galactic* scales, i.e., a local N_X – SFR relation. Due to the small number of X-ray sources (21 ULXs) detected in Obs. ID 11228, Mineo et al. (2013) were not able to study the local L_X – SFR relation in a statistically meaningful manner. Using the same SFR density image constructed by Mineo et al. (2013) (see their Sect. 4.1 for details) and following exactly the same technique (described in their Sect. 5), we now revise the spatially-resolved N_X – SFR and L_X – SFR relations for ULXs in NGC 2207/IC 2163, using the combined data from all available *Chandra* observations (Table 1). In addition, adopting the same technique, we explore the effects of age and dust extinction on the bright XRB population in NGC 2207/IC 2163 on sub-galactic scales. To characterize the dust extinction and/or age effects, we use the ratio of $8 - 1000\,\mu\text{m}$ luminosity (L_{IR}) to observed (i.e., uncorrected for attenuation effects) NUV ($2267\,\text{\AA}$) luminosity (L_{NUV}). We note that the SFR density map was constructed using *GALEX* FUV ($1516\,\text{\AA}$) and *Spitzer* MIPS $24\,\mu\text{m}$, following the calibration of Leroy et al. (2008). However, the FUV image of NGC 2207/IC 2163 has poorer statistics compared with the NUV image, which makes it less suitable for a pixel-by-pixel analysis; this is the reason why we use the NUV image to construct the $L_{\text{IR}}/L_{\text{NUV}}$ map.

For the basic IR data, we used a MIPS $24\,\mu\text{m}$ Large Field image from the "post Basic Calibrated Data" products provided by the *Spitzer* Space Telescope Data

archive¹². These are images calibrated in MJy/sr, suitable for photometric measurements. We measured the $24\,\mu\text{m}$ background in a region away from the galaxy, and subtracted it from the image. The total net counts were then converted from units of MJy/sr into Jy using a conversion factor $C_{24\,\mu\text{m}} = 1.41 \times 10^{-4}$. The monochromatic fluxes (Jy) at $24\,\mu\text{m}$ were then converted into spectral luminosities ($\text{erg s}^{-1} \text{ Hz}^{-1}$). The total IR luminosity ($8 - 1000\,\mu\text{m}$) was estimated using the relations from Bavouzet et al. (2008): $L_{\text{IR}}(L_{\odot}) = 6856 \times (\nu L_{\nu}/L_{\odot})_{24\,\mu\text{m}, \text{rest}}^{0.71}$.

We based the ultraviolet analysis on *GALEX* NUV and FUV background-subtracted intensity map data that are publicly available in the archive of GR6/GR7 Data Release¹³. These are images calibrated in units of counts per pixel per second, corrected for the relative response, with the sky background subtracted. We converted the net counts to flux using the conversion factors¹⁴ between *GALEX* count rate (cts/s) and flux ($\text{erg cm}^{-2} \text{ s}^{-1} \text{ \AA}^{-1}$): $C_{\text{NUV}} = 2.06 \times 10^{-16}$ and $C_{\text{FUV}} = 1.40 \times 10^{-15}$. The fluxes were then converted into a broad band NUV luminosity by taking the product λF_{λ} and multiplying by $4\pi D^2$.

Using the routine HASTROM, from the NASA IDL Astronomy User's Library¹⁵, we oversampled the $24\,\mu\text{m}$ image ($2.45''/\text{pix}$) so as to match the better angular resolution ($1.5''/\text{pix}$) of the *GALEX* images. This routine interpolates without adding spatial frequency information beyond the intrinsic resolution of the original image. The resulting maps, displayed in Figs. 7 and 9, have the same spatial resolution and pixel coordinates as the *GALEX* images, but are limited by the *Spitzer* resolution. Figs. 1, 3 and 9 show that IC 2163 is dustier than NGC 2207.

5. ULX AND STAR FORMATION ACTIVITY

With the SFR density image (Section 4 and Fig. 7 this paper, and Section 4.1 of Mineo et al. 2013), we now improve the spatially-resolved N_X – SFR and L_X – SFR relations for ULXs in NGC 2207/IC 2163 (Mineo et al. 2013), using the combined data from all available *Chandra* observations (Table 1). We defined a grid of uniformly spaced logarithmic bins of SFR density based on the pixel values in the SFR image (see Fig. 7). Based on the SFR density value at the position of a given X-ray source, we counted the number of sources brighter than $10^{39} \text{ erg s}^{-1}$ and their collective luminosity for each bin of SFR density. We counted the number of pixels in each bin of SFR density (over the $D25$ region) and thereby computed the corresponding integrated area. We use this area to normalize the background AGN $\log N - \log S$ function, which we take from Georgakakis et al. (2008), and thereby calculate the predicted number of background AGNs, $N_{\text{AGN}}(L > 10^{39} \text{ erg s}^{-1})$, and their equivalent luminosity, $L_{\text{AGN}}(> 10^{39} \text{ erg s}^{-1})$, above the same luminosity threshold. The respective values for the bright X-ray sources and the AGN were then subtracted to yield $N_X(L > 10^{39} \text{ erg s}^{-1})$ and $L_X(> 10^{39} \text{ erg s}^{-1})$, respectively. Dividing these values by the area under-

¹² <http://irsa.ipac.caltech.edu/applications/Spitzer/Spitzer/>

¹³ <http://galex.stsci.edu/GR6/>

¹⁴ http://galexgi.gsfc.nasa.gov/docs/galex/FAQ/counts_background.html

¹⁵ <http://idlastro.gsfc.nasa.gov/>

TABLE 3
TABLE OF THE DATA USED TO PREPARE FIGURE 8

Σ_{SFR} ($M_{\odot}/\text{yr}/\text{kpc}^2$) (1)	N_{X} (2)	L_{X} (10^{38} erg/s) (3)	N_{AGN} (4)	L_{AGN} (10^{38} erg/s) (5)	Area (kpc^2) (6)
0.0013	1	10	0.13	6.7	100
0.0027	1	41	0.25	13	190
0.0054	3	130	0.26	13	200
0.011	8	180	0.26	13	195
0.022	7	200	0.19	9.7	145
0.045	6	160	0.07	3.6	55

NOTE. — (1) Value of Σ_{SFR} at the bin center, (2) Number of ULXs per bin of Σ_{SFR} , (3) Luminosity of ULXs per bin of Σ_{SFR} , (4) Expected number of background AGNs per bin of Σ_{SFR} , (5) Expected luminosity of background AGNs per bin of Σ_{SFR} , (6) Area underlying each bin of Σ_{SFR} in kpc^2 .

lying each bin of SFR density, we obtained the surface density for X-ray point sources (source number kpc^{-2}) and luminosity density ($\text{erg s}^{-1} \text{ kpc}^{-2}$) as a function of SFR density.

These quantities are plotted against the SFR surface density in Fig. 8. Table 3 describes the data used to prepare Fig. 8. Due to ULX variability (Sect. 3.3) we now detect 28 ULXs, 7 of which were not visible in Obs. ID 11228 alone. This $\sim 30\%$ increase in ULX number, and a better average value for L_{X} , allow for an improvement in both the $N_{\text{X}} - \text{SFR}$ and $L_{\text{X}} - \text{SFR}$ relations, which is more appreciable in the latter case. Pixels with SFR density less than $6 \times 10^{-4} M_{\odot} \text{ yr}^{-1} \text{ kpc}^{-2}$ were not used as they are dominated by background noise (see Section 5 in Mineo et al. 2013). Two ULXs were located in these regions of low SFR density, therefore they are not included in our plot. In Fig. 8 we also plot the average $N_{\text{X}} - \text{SFR}$ and $L_{\text{X}} - \text{SFR}$ relations for ULXs obtained for large samples of nearby star-forming galaxies by Mineo et al. (2012a, their eqs.(20) and (22); solid lines in Fig. 8) after having converted the SFR estimate for the different IMF used in the present work (IMF as in Calzetti et al. (2007), i.e., slope -1.3 for the $0.1 - 0.5 M_{\odot}$ mass range and -2.3 for $0.5 - 120 M_{\odot}$, see Sect. 4.2 and Table 2 in Mineo et al. 2013). Similarly, we compare our results with the $N_{\text{ULX}} - \text{SFR}$ relation from Mapelli et al. (2010). The dashed line in the top panel of Fig. 8 shows their Eq. (6), which is slightly non-linear. We also plot the $N_{\text{ULX}} - \text{SFR}$ relation from Smith et al. (2012) as a dotted line, after having applied all the necessary conversions to make it compatible with the units used in Fig. 8. The latter relation is almost identical to the scaling from Mineo et al. (2012a).

Fig. 8 confirms that the multiple-galaxy-averaged relation between the total number of X-ray point sources and the integrated SFR of the host galaxy also holds on *sub-galactic* scales.

6. DUST EXTINCTION AND AGE EFFECTS ON BRIGHT XRB

Mineo et al. (2012a) investigated the correlation of $L_{\text{IR}}/L_{\text{NUV}}$ with L_{X}/SFR for HMXBs and found virtually no correlation (Spearman’s rank correlation coefficient is $r_{\text{S}} = -0.35$, corresponding to a probability of $P = 7\%$ for the null hypothesis. On the other hand, although within large error bars, the multiple-galaxy average L_{X} to SFR

ratio suggests a decreasing trend with increasing values of $L_{\text{IR}}/L_{\text{NUV}}$ (see their Fig. 11d). The ratio $L_{\text{IR}}/L_{\text{NUV}}$ is affected by both dust extinction and/or age. We investigated the possible effects of dust extinction and age on the bright XRB population in NGC 2207/IC 2163 on sub-galactic scales.

With the spatially-resolved image of $L_{\text{IR}}/L_{\text{NUV}}$ (Section 4, Fig. 9), we studied the number of X-ray point sources above the completeness luminosity and their luminosities as a function of the *local* $L_{\text{IR}}/L_{\text{NUV}}$. We applied the same pixel-by-pixel analysis to the $L_{\text{IR}}/L_{\text{NUV}}$ image that we utilized to study the local correlation between numbers and luminosities of X-ray sources and the local SFR density, which is described in Sections 4 and 5. We thereby obtained the densities $N_{\text{X}}/\text{kpc}^2$ and $L_{\text{X}}/\text{kpc}^2$ for the luminous X-ray sources and plotted these against the value of $L_{\text{IR}}/L_{\text{NUV}}$ in Fig. 10 (upper and lower panel respectively). Table 4 describes the data used to prepare Fig. 10. The figure shows a modest increase of $N_{\text{X}}/\text{kpc}^2$ and $L_{\text{X}}/\text{kpc}^2$ with $L_{\text{IR}}/L_{\text{NUV}}$ at small $L_{\text{IR}}/L_{\text{NUV}}$ values, up to $L_{\text{IR}}/L_{\text{NUV}} \sim 1$. This is followed by a decrease of the $N_{\text{X}}/\text{kpc}^2$ and $L_{\text{X}}/\text{kpc}^2$ values when $L_{\text{IR}}/L_{\text{NUV}}$ increases. Fig. 10 shows these quantities plotted against 7 discrete bins in $L_{\text{IR}}/L_{\text{NUV}}$. In order to take into account possible binning effects on the statistical significance of the observed number and luminosity density trends with $L_{\text{IR}}/L_{\text{NUV}}$, we also analyzed plots with 5 bins in $L_{\text{IR}}/L_{\text{NUV}}$. The observed trend for $N_{\text{X}}/\text{kpc}^2$ has a higher statistical significance ($\sim 3.3\sigma$ and $\sim 2.8\sigma$ for the central bins in the case of 5 bins of $L_{\text{IR}}/L_{\text{NUV}}$ vs 7 bins, respectively) than that for $L_{\text{X}}/\text{kpc}^2$ ($\sim 1.3\sigma$ and $\sim 2\sigma$ for the central bins in the case of 5-bins and 7-bins, respectively). The significance was estimated by comparing the data points and their uncertainties, with the best-fit average values: $N_{\text{X}}/\text{kpc}^2 = (1.5 \pm 0.3) \times 10^{-2}$, $L_{\text{X}}/(10^{38} \text{ erg s}^{-1})/\text{kpc}^2 = (1.5 \pm 0.3) \times 10^{-1}$ (7-bin plot). We view all this as tentative evidence for a smoothly peaked dependence of $N_{\text{X}}/\text{kpc}^2$ and $L_{\text{X}}/\text{kpc}^2$ on $L_{\text{IR}}/L_{\text{NUV}}$.

The $L_{\text{IR}}/L_{\text{NUV}}$ ratio may also be seen as a rough indicator of the timescale of the star formation event. The UV emission originating from the photospheres of O and B stars is absorbed and re-emitted in the IR band by dust grains heated by the embedded young ionizing stars. The IR should trace somewhat younger star formation (< 10 Myr, Calzetti et al. 2007), while UV traces older star formation (30 – 100 Myr, Calzetti et al. 2005), see also Kennicutt & Evans (2012). This might suggest, as a rough timescale, that at $L_{\text{IR}}/L_{\text{NUV}} < 1$, the age may be $\gtrsim 10$ Myr, and therefore, the trend in Fig. 10 might be tentatively ascribed to an age effect on the bright XRB formation and evolution. The UV dominates where the dust absorption is very low. In Milky Way type galaxies, this means that the molecular clouds have dissipated, or at least the stars have moved out of the clouds. To summarize: i) high L_{IR} could mean such high dust obscuration that we fail to detect some X-ray sources. ii) High L_{NUV} could mean an older stellar population which has become free of dust. iii) The $L_{\text{IR}}/L_{\text{NUV}}$ ratio could indicate age which might, importantly, affect how many ULXs have already evolved away. Additionally, there are further complications due to the chemical composition,

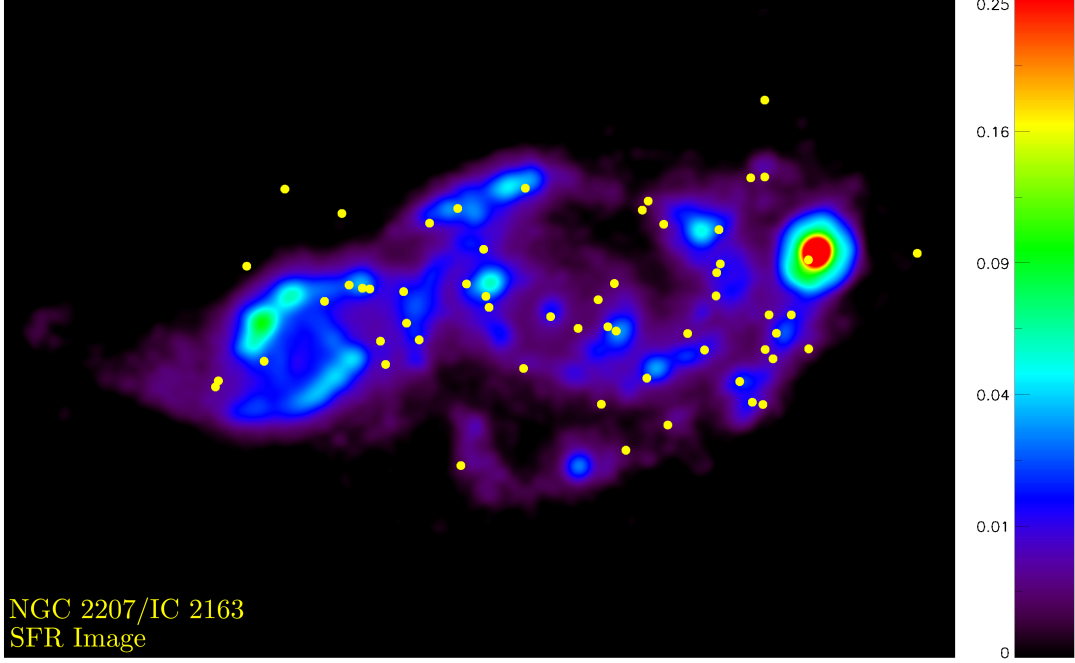


FIG. 7.— Star formation rate density map for the colliding galaxies NGC 2207/IC 2163. This image was generated from a linear combination of *GALEX* FUV and Spitzer $24\mu\text{m}$ images according the prescription of Leroy et al. (2008). The units are $M_{\odot} \text{ yr}^{-1} \text{ kpc}^{-2}$. The filled yellow circles mark the locations of the 57 X-ray sources detected in the four combined *Chandra* observations, above the completeness limit ($3.4 \times 10^{38} \text{ erg s}^{-1}$; see Table 2). For details see Sect. 4.1 in Mineo et al. (2013).

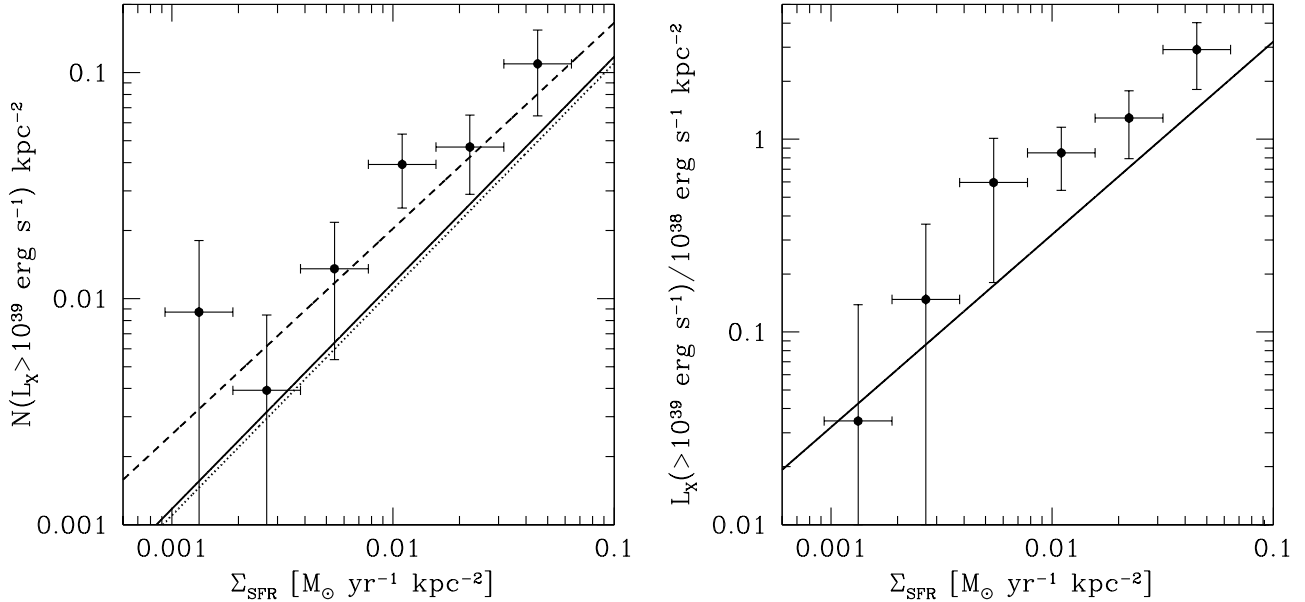


FIG. 8.— Relation between the *local* SFR density in NGC 2207/IC 2163 ($M_{\odot} \text{ yr}^{-1} \text{ kpc}^{-2}$) and the number density (N_X/kpc^2 , left panel) and luminosity density (L_X/kpc^2 , right panel) of ULXs. Both of these quantities have been corrected for the contribution of background AGNs. The SFR density was computed from the Leroy et al. (2008) algorithm as described in Sect. 4. The solid curves are the multiple-galaxy-wide average $N_X - \text{SFR}$ (left panel) and $L_X - \text{SFR}$ (right panel) relations for ULXs obtained in Mineo et al. (2012a, their eqs.(20) and (22) respectively). These curves are shown for comparison after having been rescaled to match the IMF assumption in the SFR recipe from Leroy et al. (2008). The corresponding ULX vs. SFR relation from Mapelli et al. (2010, their Eqn. 6) is shown as a dashed line in the left panel. The dotted line represents the $N_{\text{ULX}} - \text{SFR}$ relation from Smith et al. (2012).

which we do not address in the present work.

Interpreting the trend observed in Fig. 10 as an effect of age or star formation timescale, we see that the number of bright XRBs and their luminosity peaks at ≈ 10 Myr, i.e., around the epoch where young stars are escaping from the dust clouds that enshroud them. We note that these qualitative conclusions are in agreement with the results found by Swartz et al. (2009) for a large sample of ULXs detected in 58 nearby galaxies. They found that the most luminous ULXs (or equivalently, the most common phases of very high mass transfer) are biased toward early B-type donors with an initial mass of $\approx 10 - 15 M_{\odot}$ and an age $\sim 10 - 20$ Myr, perhaps at the stage where the B star expands to become a blue supergiant. Similarly, an age of $\approx 10 - 20$ Myr was inferred for the stars around NGC 4559 X-1 by Soria et al. (2005) and ≈ 20 Myr for those around NGC 1313 X-2 by Grisé et al. (2008).

However, this interpretation remains mostly tentative. Not only do the data points in Fig. 10 have rather large error bars, but there is also some uncertainty introduced as a result of the pixel interpolation applied to obtain the $L_{\text{IR}}/L_{\text{NUV}}$ map (see Sect. 4). Moreover, the $24 \mu\text{m}$ emission may depend on dust geometry and the conversion from $24 \mu\text{m}$ to total IR luminosity has a very large uncertainty. The $L_{\text{IR}}/L_{\text{NUV}}$ is not a perfect age indicator, but it should be at least statistically meaningful.

The $L_{\text{IR}}/L_{\text{NUV}}$ ratio of galaxies also depends upon metallicity, with lower metallicity systems having less dust and therefore lower $L_{\text{IR}}/L_{\text{NUV}}$ (see, e.g., Kunth & Oumstlin 2000; Johnson et al. 2007; Basu-Zych et al. 2013b); therefore, the range $L_{\text{IR}}/L_{\text{NUV}} < 1$ may also show the low metallicity regions of NGC 2207/IC 2163. Based on the emission line analysis of H II regions in interacting galaxies, Rupke et al. (2010) found that the metallicity in NGC 2207/IC 2163 is in the range $12 + \log([O/H]) \approx 8.8 - 9.2$ and they show that IC 2163 hosts regions with, on average, higher metallicity ($12 + \log([O/H]) \gtrsim 9$) than those in NGC 2207 ($12 + \log([O/H]) \lesssim 9$). On the other hand, a full range of ≈ 0.4 dex may not be enough in terms of the implied dust to gas ratio, suggesting that in the case of NGC 2207/IC 2163 the effects of metallicity may not be important. We may conclude that either bright XRBs have not yet formed in the dustier galaxy (IC 2163), or they are hidden by high extinction (in agreement with the results of Smith et al. 2012; Luangtip et al. 2014).

7. DIFFUSE X-RAY EMISSION

Star-forming galaxies are known to emit significant amounts of X-rays at \sim sub-keV temperatures (typically in the range of 0.2–0.3 keV, sometimes with evidence of a second thermal component at ~ 0.7 keV), due to hot ionized gas. The luminosity of the diffuse thermal X-ray emission correlates with the SFR of the host galaxy. The gas is thought to be in a state of outflow, driven by the collective effects of supernovae and winds from massive stars (Chevalier & Clegg 1985; Strickland et al. 2000, 2004; Grimes et al. 2005; Tüllmann et al. 2006; Owen & Warwick 2009; Yukita et al. 2012; Mineo et al. 2012b; Li & Wang 2013).

7.1. Isolating the hot ISM in NGC 2207/IC 2163

TABLE 4
TABLE OF THE DATA USED TO PREPARE FIGURE 10

$L_{\text{IR}}/L_{\text{NUV}}$	N_{X}	L_{X} (10^{38} erg/s)	N_{AGN}	L_{AGN} (10^{38} erg/s)	Area (kpc^2)
(1)	(2)	(3)	(4)	(5)	(6)
0.16	4	59	1.3	30	455
0.32	12	230	1.5	35	525
0.67	16	200	1.3	31	465
1.4	17	200	0.9	21	315
2.9	4	50	0.28	6.7	100
6.1	1	4	0.11	2.7	40
13	1	19	0.039	0.91	15

NOTE. — (1) Value of $L_{\text{IR}}/L_{\text{NUV}}$ at the bin center, (2) Number of X-ray binaries above the completeness luminosity per bin of $L_{\text{IR}}/L_{\text{NUV}}$, (3) Luminosity of X-ray binaries per bin of $L_{\text{IR}}/L_{\text{NUV}}$, (4) Expected number of background AGNs per bin of $L_{\text{IR}}/L_{\text{NUV}}$, (5) Expected luminosity of background AGNs per bin of $L_{\text{IR}}/L_{\text{NUV}}$, (6) Area underlying each bin of $L_{\text{IR}}/L_{\text{NUV}}$ in kpc^2 .

Recently, Mineo et al. (2012b) isolated the contribution of hot, diffuse ISM in a sample of 21 local, star-forming galaxies. They took special care of various systematic effects and controlled the contamination by “spill-over” counts from bright resolved compact sources to the diffuse emission. Here we use the same procedures to isolate the truly diffuse emission due to the hot ISM from contaminating components and to obtain its luminosity.

We first searched for the optimal size of the regions to be used to remove the point source counts from the image and minimize the contamination by “spill-over” counts. We used the same procedure described in Sect. 2 to search for point-like sources in the soft (0.5–2 keV), hard (2–8 keV), and total (0.5–8 keV) energy bands. For each source, we used the information about the shape of the point spread function (PSF) at the source position to determine the radius of the circular region containing 90% of the source counts, i.e., $R_{90\% \text{ PSF}}$. From the source lists obtained in each energy band, we created a set of source regions having radii ranging from $0.5 R_{90\% \text{ PSF}}$ to $3.5 R_{90\% \text{ PSF}}$ with a step of 0.1. A corresponding set of diffuse emission images was created for each observation of NGC 2207/IC 2163, adopting the following method. We removed the source regions from the image and, using the CIAO task `dmfilth` (POISSON method), we filled in the holes left by the source removal with pixel values interpolated from surrounding background regions. The background region for this interpolation purpose was defined as a circle with radius 3 times the radius of the source region. We ensured that the chosen background annuli did not contain neighboring point sources. For each background region listed in the input file, we subtracted all the overlapping neighboring point source regions and merged them into a single source removal region. For each of the resulting images, we estimated the count rate within the $D25$ ellipse using the CIAO task `dmextract` and plotted it against the radius of the removed-source region. This plot showed a sharp decrease of the count rate at small source radii $\leq R_{90\% \text{ PSF}}$, followed by a flattening of the curve at $R > 1.5 - 2 R_{90\% \text{ PSF}}$. We found that on average the difference between excluding source regions with $R = 1.5 R_{90\% \text{ PSF}}$ and $R = 2 R_{90\% \text{ PSF}}$ is only $\sim 4\%$ of the background-subtracted soft band count rate. Based

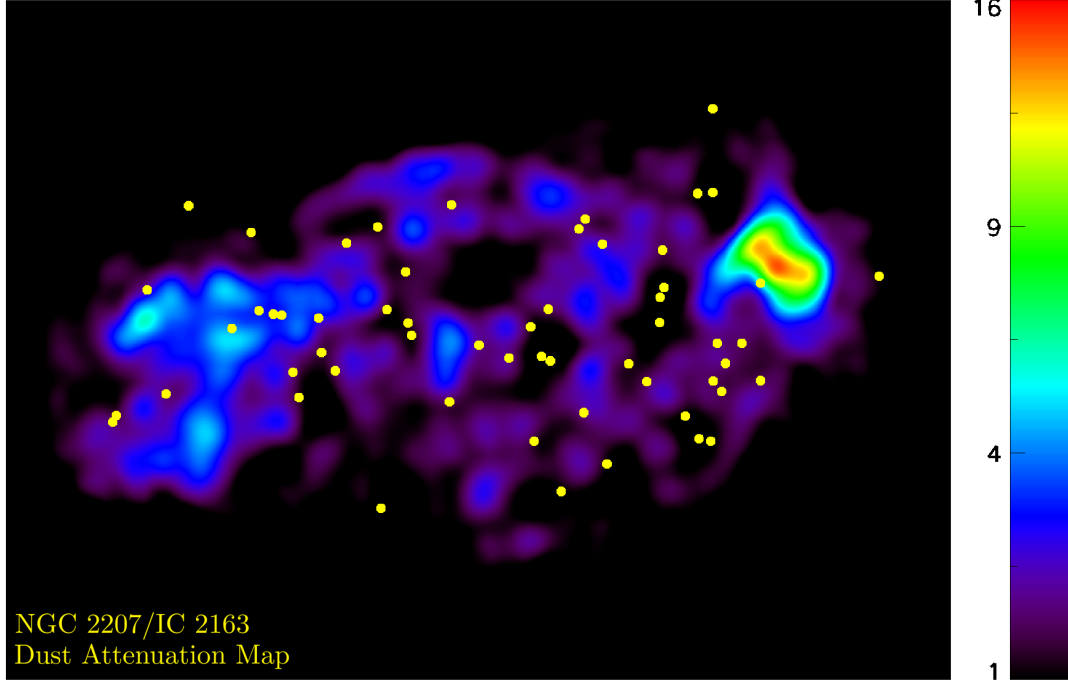


FIG. 9.— Map of $L_{\text{IR}}/L_{\text{NUV}}$ for NGC 2207/IC 2163 obtained by combining *GALEX* FUV and Spitzer $24\mu\text{m}$ images according the prescription described in Sect. 4. The small yellow circles mark the locations of the 57 X-ray sources detected in the four combined *Chandra* observations, above the completeness limit of $3.4 \times 10^{38} \text{ erg s}^{-1}$ (Table 2).

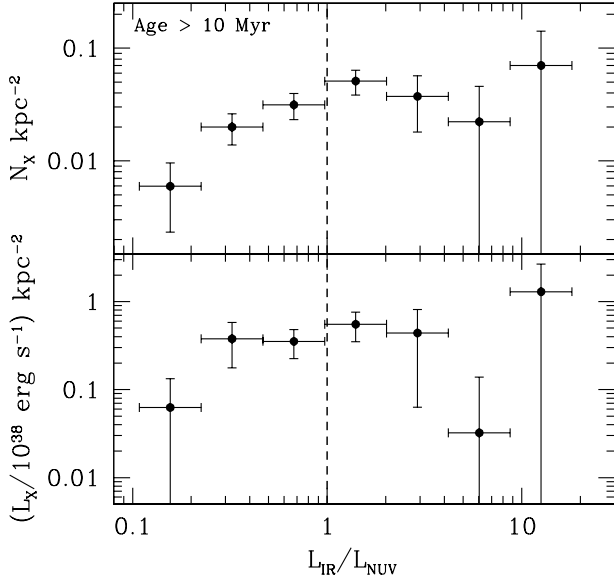


FIG. 10.— Relation between the *local* $L_{\text{IR}}/L_{\text{NUV}}$ in NGC 2207/IC 2163, as indicated by $L_{\text{IR}}/L_{\text{NUV}}$, and the number density N_X/kpc^2 (upper panel) and luminosity density L_X/kpc^2 (lower panel) of X-ray sources detected above our completeness luminosity threshold in the combined image ($3.4 \times 10^{38} \text{ erg s}^{-1}$). Both of these quantities have been corrected for the contribution of background AGNs, see Sect. 6 for details.

on this analysis, we adopted a source region radius of $R = 1.5 R_{90\% \text{ PSF}}$ to minimize the contamination of dif-

fuse emission by point-source counts without compromising the statistics for the diffuse emission itself. The diffuse emission spectrum was extracted, in each individual observation, from the $D25$ region, after having removed the circular regions with $R = 1.5 R_{90\% \text{ PSF}}$ for all detected point sources.

The background spectrum was extracted, in each observation, from a region defined by the whole *Chandra* chip outside $1.3 \times D25$, to avoid contamination from true diffuse emission in the outskirts of the $D25$ region and to retain good count statistics for the background spectrum itself. This takes into account both the instrumental and cosmic X-ray background.

The co-added spectrum of diffuse X-ray emission from all four observations in the 0.5–8 keV band is shown in Fig. 11, along with the composite point source spectrum that was obtained in Sect. 2.3.

7.2. Spectral analysis

Using the `combine_spectra` script we co-added the four spectra extracted from the individual observations. We binned the composite spectrum so as to have a minimum of 20 counts per channel in order to apply χ^2 statistics. The spectral analysis was performed with XSPEC v. 12.7.1b.

The co-added background-subtracted spectrum of diffuse X-ray emission was first modeled in the 0.5–8 keV band, with two components, thermal (`mekal`) and power-law, to which we applied photo-electric absorption. We used two absorbing components (`phabs(1)*phabs(2)`), one fixed to the Galactic value, $N_H = 8.8 \times 10^{20} \text{ cm}^{-2}$ (Kalberla et al. 2005). The other one was instead left free to constrain the absorption local to NGC 2207/IC 2163. Overall the model provides a good description of the full-

TABLE 5
DIFFUSE AND POINT SOURCE COUNT RATE RATIOS

Energy band	f_{diff}	f_{XRBs}	$f_{\text{diff}}/f_{\text{XRBs}}$
(1)	(2)	(3)	(4)
0.5–8 keV	38 ± 1.3	31 ± 0.71	1.2 ± 0.051
0.5–2 keV	32 ± 0.94	20 ± 0.57	1.6 ± 0.064
0.5–1 keV	18 ± 0.65	4.4 ± 0.27	4.1 ± 0.29
1–2 keV	13 ± 0.67	16 ± 0.5	0.86 ± 0.051
2–3 keV	2 ± 0.42	4.7 ± 0.27	0.42 ± 0.094
3–8 keV	3.8 ± 0.84	5.6 ± 0.3	0.67 ± 0.15

NOTE. — (1) Energy band, (2) net count rate for the spectrum of diffuse emission, (3) net count rate for the spectrum of resolved point sources, (4) ratio between diffuse emission and resolved point source count rates. See Sect. 7 for details.

band spectrum with $\chi^2 = 214$ for 208 degrees of freedom (reduced $\chi^2 = 1.03$). The power-law model accommodates the emission at $E > 1 - 1.5$ keV. This can be visually recognized in Fig. 11 and can also be noted by looking at the ratios between diffuse and point source count rates in several bands listed in Table 5. Since the contribution of resolved point sources was excluded from the diffuse spectrum, this power-law component may be due to unresolved accreting compact sources (see, e.g., Mineo et al. 2012b). The best fit photon index is $\Gamma = 1.83^{+0.39}_{-0.36}$, which makes it consistent with unresolved compact objects, but it is not very well constrained (note the uncertainties) due to the weak count statistics of the diffuse spectrum in the 2–8 keV band. Our analysis suggests that the local absorption in NGC 2207/IC 2163 is $N_{\text{H}} = (2.0 \pm 1.4) \times 10^{21} \text{ cm}^{-2}$, in agreement with the column density obtained for the co-added point source spectrum (see Sect. 2.3). The thermal component fits the spectrum rather well at $E < 1$ keV and its best-fit plasma temperature is well constrained: $kT = 0.28^{+0.05}_{-0.04}$ keV, for solar metal abundances.

We repeated the fit over only the 0.5–1 keV band, where the thermal emission dominates. The soft spectrum is well described by an absorbed thermal model, with $\chi^2 = 35.5$ for 30 degrees of freedom (reduced $\chi^2 = 1.18$). The local absorbing component was constrained to $N_{\text{H}} = (3.3 \pm 1.1) \times 10^{21} \text{ cm}^{-2}$, in agreement with the values reported above as well with that obtained for the point source spectrum. The best-fit value for the plasma temperature is $kT = 0.25^{+0.04}_{-0.03}$ keV. Although the soft band emission, 0.5–2 keV, is not totally dominated by diffuse gas, these spectral characteristics are typical for normal star-forming and starburst galaxies.

7.3. X-ray luminosity of the hot ISM

The 0.5–2 keV X-ray luminosity of the thermal plasma, calculated based on the full-band fitting, corrected for Galactic absorption, is $L_{0.5-2\text{keV}}^{\text{mekal}} = 2.8 \times 10^{40} \text{ erg s}^{-1}$, which is a factor of ~ 2.3 larger than the average thermal luminosity produced per unit SFR in local star-forming galaxies (Mineo et al. 2012b, see their Eq. (2)).

This calculation was based on the integrated SFR of NGC 2207/IC 2163 ($23.7 M_{\odot} \text{ yr}^{-1}$, see also Mineo et al. 2013) estimated using observed (i.e. uncorrected for dust absorption) NUV and total, 8–1000 μm , IR, assuming a Salpeter initial mass function (IMF) from 0.1 to 100 M_{\odot}

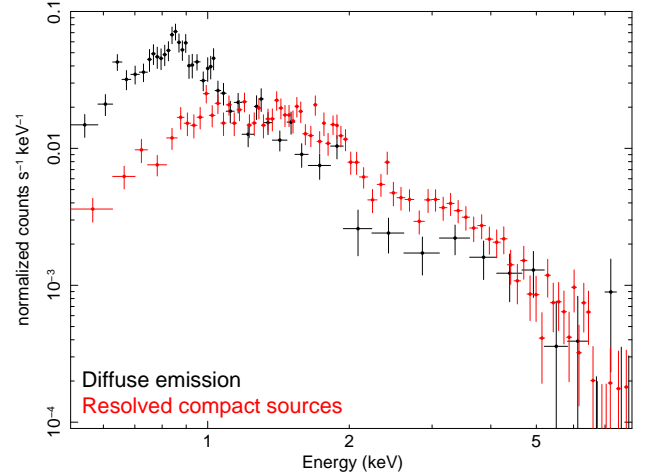


FIG. 11.— The co-added X-ray spectra of diffuse emission (black, Sect. 7) and resolved point sources (red, Sect. 2.3) over the four individual observations in the full (0.5–8 keV) band. Both spectra were extracted from the D25 ellipse of NGC 2207/IC 2163 and are binned in order to have a minimum of 20 counts per channel. The hot ISM dominates the emission in the 0.5–1 keV band.

(Iglesias-Páramo et al. 2006). This is one of the best SFR estimators for nearby galaxies, and is the same proxy as used by Mineo et al. (2012a,b), providing the most robust value for the integrated SFR of NGC 2207/IC 2163, and full consistency when we compare our results with previous, more extensive work.

The measured value of $L_{0.5-2\text{keV}}^{\text{mekal}}/\text{SFR}$ is also a factor of ~ 1.5 larger than the average 0.5–2 keV luminosity of the HMXBs per unit SFR (Mineo et al. 2012a), in full agreement with the values in Table 5, and corresponds to $\sim 40\%$ of the integrated luminosity of all point sources detected above the completeness limit for the combined observations in the 0.5–8 keV band (listed in Table 2). Such a result is about 10% larger than what is typically in local star-forming galaxies, but within the dispersion. After having corrected for both Galactic and local absorption, we obtained the intrinsic luminosity of the hot ISM, $L_{0.5-2\text{keV}}^{\text{mekal,int}} = 7.9 \times 10^{40} \text{ erg s}^{-1}$.

After having rescaled our SFR estimate to a Kroupa IMF, the intrinsic luminosity of the hot ISM obtained above is in the same range as the values found by Smith et al. (2014, their Table 12, only including sources with extended X-ray emission) for a sample of hinge clumps in five interacting galaxies, and similar to that for the Antennae.

8. SUMMARY AND CONCLUSIONS

We have presented a comprehensive study of the total X-ray emission from the colliding galaxy pair NGC 2207/IC 2163.

We repeated our correlation study between the *local* SFR in NGC 2207/IC 2163 and the number and X-ray luminosity of the ULXs with improved significance with respect to our pilot study (Mineo et al. 2013), which was based on only one (Obs. ID 11228) of the four observations utilized in the present work. Due to ULX variability (Sect. 3.3) we now detect 28 ULXs, 7 of which were not visible previously. This $\sim 30\%$ increase in ULX number

allows for an improvement in both the spatially-resolved $N_X - \text{SFR}$ and $L_X - \text{SFR}$ relations, which is most evident in the latter case. We confirm that the global relation between the *number* of X-ray point sources and the integrated SFR of the host galaxy also holds on *local* scales within a given galaxy. Thanks to the improved statistics utilized in the present analysis, we can now show that the relation between *X-ray luminosity* and *local* SFR is also in general agreement with the multiple-galaxy-wide average relation between the cumulative luminosity of ULXs and the integrated SFR.

We investigated the long-term flux and spectral variability of the ULX population and found that 12 sources out of 57 ($\sim 20\%$ including the AGN at the center of NGC 2207) show significant long-term variability ($S_{\text{flux}} > 3$; see Sect. 3.3). Of these, 7 are transient source candidates. The ratio between maximum and minimum count rate ranges between 2 and 3.8 for the variable sources, but between ~ 34 and ~ 72 for the transient source candidates. One of the variable sources (#41 in Tables 6 and A5) is the central AGN in NGC 2207. One of the transient sources (#22 in Tables 6 and A5), is associated ($0.11''$ separation) with the supernova SN 2013ai. We find no evidence for X-ray spectral changes in connection with the ULX's flux variability. All the ULXs (except the one associated with SN 2013ai) have a soft spectrum during all four observations. Such behavior has been observed when the flux variability ranges over only a factor of a few.

We cross checked the coordinates of 17 optical “super-star clusters” (SSC, mass $1\text{--}20 \times 10^4 M_\odot$) identified with *HST* as well as the coordinates of 225 *Spitzer* 8-micron clumps with the positions of the 74 X-ray sources detected within the D25 ellipse in the co-added *Chandra* image. Within a $1.5''$ tolerance limit, we found that only one young SSC is coincident with a bright XRB ($L_X < 10^{39} \text{ erg s}^{-1}$); by contrast, we found a statistically significant set of $\sim 1/3$ of our X-ray sources which align with *Spitzer* 8 μm -detected young star complexes, and half of the matching sources are ULXs. Among the matches there are two SNe, SN 1999ec and SN 2013ai, as well as the extended X-ray source at the location of the dusty starburst region called “*feature i*”.

We report that our X-ray source #18 corresponds to source “X1” in Kaufman et al. (2012), whose nature was still uncertain. The latter authors interpreted their source X1 as a possible radio SN, a SNR, or a background quasar. The significant variability and spectral hardness of our X-ray source #18 are incompatible with an AGN and, according to its luminosity, $L_X > 10^{39} \text{ erg s}^{-1}$ in all *Chandra* pointings, we conclude that the source is a ULX.

We constructed the X-ray luminosity function of the bright X-ray point sources in each individual observation and found that the best-fitting slopes are in agreement with each other within the uncertainties (Table 2). This suggests that the X-ray variability exhibited by about 20% of the detected sources does not significantly influence their XLFs. We also obtained the XLF from the four combined *Chandra* observations. The best-fitting model for the average XLF is a power-law with slope $\alpha = 0.66 \pm 0.04$ (1.66 in differential form) and an exponential cut-off at $L_o = (3.39 \pm 0.28) \times 10^{39} \text{ erg s}^{-1}$. The

slope is in full agreement with that of the average XLF for HMXBs and the exponential cutoff in our model may correspond to the roll-off of the bright end of a more extended power-law distribution with slope 1.6.

We studied the possible effects of dust extinction and age on a bright XRB population in NGC 2207/IC 2163 on sub-galactic scales. We applied the same technique as that used to obtain the image of the SFR density. To characterize the dust extinction within the galaxy pair, we used the ratio of $8 - 1000 \mu\text{m}$ luminosity (L_{IR}) to observed (i.e., uncorrected for attenuation effects) NUV luminosity (L_{NUV} at 2267 \AA). We found that the number and luminosity of bright XRBs show a trend with the *local* $L_{\text{IR}}/L_{\text{NUV}}$ ratio. In particular, we observe a peak in the N_X and L_X distributions at $L_{\text{IR}}/L_{\text{NUV}} \sim 1$, which is more significant for N_X . The peak may be tentatively interpreted as an effect of the different star formation timescales traced by the IR and NUV proxies, and we speculate that at $L_{\text{IR}}/L_{\text{NUV}} \approx 1$, the age of the underlying stellar population may be around 10 Myr. That these qualitative conclusions are in agreement with more quantitative previous results suggests that the most luminous ULXs are biased towards donor stars having an age $\sim 10 - 20$ Myr (Soria et al. 2005; Grisé et al. 2008; Swartz et al. 2009). However, this interpretation still remains somewhat tentative.

We disentangled and compared the X-ray spectra of the diffuse emission with the population of bright XRBs hosted by NGC 2207/IC 2163. The hot ISM has a temperature $kT = 0.28_{-0.04}^{+0.05} \text{ keV}$, assuming solar metal abundances, and dominates the overall X-ray output of NGC 2207/IC 2163 at $E \lesssim 1 \text{ keV}$. Unresolved accreting compact objects most likely dominate the diffuse X-ray emission at $E \gtrsim 1 \text{ keV}$.

The co-added spectrum of resolved X-ray point sources is well described by an absorbed power-law with index $\Gamma = 1.95 \pm 0.08$, consistent with the centroid of the power law photon index distribution for luminous X-ray compact sources in star-forming galaxies, $\Gamma = 1.97 \pm 0.11$ (Swartz et al. 2004).

The 0.5–2 keV X-ray luminosity of the thermal plasma, based on the full-band fitting, and corrected for both Galactic and local absorption, is $L_{0.5-2\text{keV}}^{\text{mekal,int}} = 7.9 \times 10^{40} \text{ erg s}^{-1}$, which is a factor of ~ 2.3 larger than the average thermal luminosity produced per unit SFR in local star-forming galaxies and corresponds to $\sim 100\%$ of the collective luminosity of all point sources detected above the completeness limit for the combined observations ($7.8 \times 10^{40} \text{ erg s}^{-1}$). Such a result is about 10% larger than what is typical in local star-forming galaxies, but within the dispersion of values. After having subtracted the estimated contribution of background AGNs, the total X-ray output of NGC 2207/IC 2163 is $1.5 \times 10^{41} \text{ erg s}^{-1}$. The corresponding total, integrated SFR is $23.7 M_\odot \text{ yr}^{-1}$.

We thank the anonymous referee for helpful suggestions that greatly improved this paper. We acknowledge support from the NASA’s Astrophysics Data Analysis Program (ADAP) grant NNH13CH56C and by NASA *Chandra* grant GO3-14092A. We acknowledge Steven

TABLE 6
NGC2207/IC2163: ULX VARIABILITY

Source	α_{J2000} (deg)	δ_{J2000} (deg)	Obs. ID 11228		Obs. ID 14914		Obs. ID 14799		Obs. ID 14915		S_{flux}
			Photon flux (10^{-7} ph cm $^{-2}$ s $^{-1}$)	HR (cts)	Photon flux (10^{-7} ph cm $^{-2}$ s $^{-1}$)	HR (cts)	Photon flux (10^{-7} ph cm $^{-2}$ s $^{-1}$)	HR (cts)	Photon flux (10^{-7} ph cm $^{-2}$ s $^{-1}$)	HR (cts)	
(1)	(2)	(3)	(4)	(5)	(6)	(7)	(8)	(9)	(10)	(11)	(12)
51	94.10071	-21.3865	16 ± 10	-1.00 ± 0.63	0.91 ± 3.4	-1.00 ± 4.28	30 ± 12	-0.08 ± 0.46	28 ± 7.9	-0.80 ± 0.25	3.2
31	94.08431	-21.3851	38 ± 12	-0.41 ± 0.32	≤ 3.7	...	2.4 ± 6.5	1.00 ± 3.75	1.3 ± 3.5	1.00 ± 4.30	3.1
37	94.08675	-21.3808	≤ 3.7	...	49 ± 9.7	-0.33 ± 0.20	33 ± 13	0.16 ± 0.43	31 ± 8.1	-0.67 ± 0.25	4.7
14	94.07177	-21.3807	81 ± 16	-0.55 ± 0.19	87 ± 13	-0.23 ± 0.15	140 ± 23	-0.18 ± 0.17	52 ± 10	-0.42 ± 0.20	3.4
74	94.12505	-21.3792	25 ± 11	-0.83 ± 0.43	41 ± 9.8	-0.77 ± 0.21	20 ± 11	-0.74 ± 0.62	≤ 3.9	...	3.9
22*	94.07649	-21.3758	≤ 3.6	...	≤ 3.6	...	93 ± 19	0.71 ± 0.18	0.91 ± 3.4	-1.00 ± 4.95	4.8
2	94.06618	-21.3757	180 ± 22	-0.36 ± 0.12	170 ± 17	-0.32 ± 0.10	80 ± 18	-0.43 ± 0.23	49 ± 10	-0.38 ± 0.21	6.3
41†	94.09177	-21.3727	140 ± 20	0.76 ± 0.12	110 ± 14	0.56 ± 0.13	93 ± 21	0.79 ± 0.20	200 ± 18	0.81 ± 0.07	3.7
46	94.09788	-21.3719	1 ± 5.3	1.00 ± 4.37	50 ± 9.8	-0.12 ± 0.21	74 ± 18	-0.12 ± 0.26	3.1 ± 4.2	0.83 ± 2.00	4.4
62	94.11047	-21.3701	23 ± 10	-0.80 ± 0.44	42 ± 9.2	-0.15 ± 0.23	41 ± 14	-0.19 ± 0.37	88 ± 13	-0.28 ± 0.15	4
18	94.07493	-21.3678	68 ± 15	-0.62 ± 0.21	33 ± 8.4	-0.26 ± 0.27	28 ± 12	-0.37 ± 0.49	19 ± 6.7	-0.44 ± 0.38	3
66	94.11249	-21.3632	≤ 3.9	...	29 ± 7.9	-0.34 ± 0.29	14 ± 9.6	-0.20 ± 0.79	2.7 ± 3.9	-1.00 ± 1.87	3.3

Footnote (1) Source number based on Table A5. (2) Right Ascension (RA). (3) Declination (Dec). (4), (6), (8), (10) Net photon fluxes in the 0.5–8 keV band, in units of 10^{-7} cts s $^{-1}$. (5), (7), (9), (11) Hardness ratios, computed with eq. (1). (12) Significance of long-term flux variability, computed with eq. (4). † Central Active Galactic Nucleus, * SN 2013ai (0.11" match)

Note: (1) Source number based on Table A5, (2) Right Ascension (RA), (3) Declination (Dec), (4), (6), (8), (10) Net photon fluxes in the 0.5–8 keV band, in units of 10^{-7} cts s $^{-1}$; (5), (7), (9), (11) Hardness ratios, computed with eq. (1). (12) Significance of long-term flux variability, computed with eq. (4). † Central Active Galactic Nucleus, * SN 2013ai (0.11'' match)

Willner, Luca Cortese, Bret Lehmer and Antara Basu-Zych for insightful discussions on dust extinction, star formation and their relation with the starburst age. We are grateful to Michele Kaufman and Debra Elmegreen who kindly supplied us with the coordinates of the 17 super star clusters that they had identified in the HST image, and for further discussions. We made use of *Chandra* archival data and software provided by the *Chandra* X-ray Center (CXC) in the application package CIAO. We also utilized the software tool SAOImage DS9, developed by the Smithsonian Astrophysical Observatory. The FUV, 3.6 μm , and 24 μm images were taken from the *GALEX* and *Spitzer* archives, respec-

tively. The *Spitzer Space Telescope* is operated by the Jet Propulsion Laboratory, California Institute of Technology, under contract with NASA. *GALEX* is a NASA Small Explorer, launched in 2003 April. We also made use of data products from the Two Micron All Sky Survey (2MASS), which is a joint project of the University of Massachusetts and the Infrared Processing and Analysis Center/California Institute of Technology, funded by NASA and the National Science Foundation. Helpful information was found in the NASA/IPAC Extragalactic Database (NED) which is operated by the Jet Propulsion Laboratory, California Institute of Technology, under contract with the National Aeronautics and Space Administration.

REFERENCES

- Arnett, W. D. 1982, *ApJ*, 254, 1
 Basu-Zych, A. R., Lehmer, B. D., Hornschemeier, A. E., et al. 2013, *ApJ*, 762, 45
 Basu-Zych, A. R., Lehmer, B. D., Hornschemeier, A. E., et al. 2013, *ApJ*, 774, 152
 Bauer, F. E., Alexander, D. M., Brandt, W. N., et al. 2004, *AJ*, 128, 2048
 Bavouzet, N., Dole, H., Le Floc'h, E., et al. 2008, *A&A*, 479, 83
 Bell, E. F. 2003, *ApJ*, 586, 794
 Bhattacharya, D., & van den Heuvel, E. P. J. 1991, *Phys. Rep.*, 203, 1
 Bloom, J. S., Kulkarni, S. R., Price, P. A., et al. 2002, *ApJ*, 572, L45
 Bonnell, I. A., Dobbs, C. L., Robitaille, T. P., & Pringle, J. E. 2006, *MNRAS*, 365, 37
 Brorby, M., Kaaret, P., & Prestwich, A. 2014, arXiv:1404.3132
 Calzetti, D., Kennicutt, R. C., Jr., Bianchi, L., et al. 2005, *ApJ*, 633, 871
 Calzetti, D., Kennicutt, R. C., Engelbracht, C. W., et al. 2007, *ApJ*, 666, 870
 Chevalier R. A., Clegg A. W., 1985, *Natur*, 317, 44
 Colbert, E. J. M., & Mushotzky, R. F. 1999, *ApJ*, 519, 89
 Copperwheat, C., Cropper, M., Soria, R., & Wu, K. 2005, *MNRAS*, 362, 79
 David, L. P., Jones, C., & Forman, W. 1992, *ApJ*, 388, 82
 Done, C., & Gierliński, M. 2003, *MNRAS*, 342, 1041
 Elmegreen, B. G., Kaufman, M., Struck, C., et al. 2000, *AJ*, 120, 630
 Elmegreen, D. M., Kaufman, M., Elmegreen, B. G., et al. 2001, *AJ*, 121, 182
 Elmegreen, D. M., Elmegreen, B. G., Kaufman, M., et al. 2006, *ApJ*, 642, 158
 Farrell, S. A., Webb, N. A., Barret, D., Godet, O., & Rodrigues, J. M. 2009, *Nature*, 460, 73
 Feng, H., & Soria, R. 2011, *New Astronomy Reviews*, 55, 166
 Fridriksson, J. K., Homan, J., Lewin, W. H. G., Kong, A. K. H., & Pooley, D. 2008, *ApJS*, 177, 465
 Gao, Y., Wang, Q. D., Appleton, P. N., & Lucas, R. A. 2003, *ApJ*, 596, L171
 Georgakakis, A., Nandra, K., Laird, E. S., Aird, J., & Trichas, M. 2008, *MNRAS*, 388, 1205
 Gehrels, N. 1986, *ApJ*, 303, 336
 Gladstone, J. C., Roberts, T. P., & Done, C. 2009, *MNRAS*, 397, 1836
 Grimm, H.-J., Gilfanov, M., & Sunyaev, R. 2003, *MNRAS*, 339, 793
 Grimes, J. P., Heckman, T., Strickland, D., & Ptak, A. 2005, *ApJ*, 628, 187
 Grisé, F., Pakull, M. W., Soria, R., et al. 2008, *A&A*, 486, 151
 Hamuy, M., Trager, S. C., Pinto, P. A., et al. 2000, *AJ*, 120, 1479
 Hao, C.-N., Kennicutt, R. C., Johnson, B. D., et al. 2011, *ApJ*, 741, 124
 Heida, M., Jonker, P. G., Torres, M. A. P., et al. 2014, *MNRAS*, 442, 1054
 Higdon, J. L. 1995, *ApJ*, 455, 524
 Hirashita, H., Buat, V., & Inoue, A. K. 2003, *A&A*, 410, 83
 Iglesias-Páramo, J., Buat, V., Donas, J., Boselli, A., & Milliard, B. 2004, *A&A*, 419, 109
 Iglesias-Páramo, J., Buat, V., Takeuchi, T. T., et al. 2006, *ApJS*, 164, 38
 Leroy, A. K., Walter, F., Brinks, E., et al. 2008, *AJ*, 136, 2782
 Li, J.-T., & Wang, Q. D. 2013, *MNRAS*, 428, 2085
 Liu, J.-F., Bregman, J. N., & Seitzer, P. 2002, *ApJ*, 580, L31
 Liu, Q. Z., van Paradijs, J., & van den Heuvel, E. P. J. 2006, *A&A*, 455, 1165
 Liu, J.-F., Bregman, J. N., Bai, Y., Justham, S., & Crowther, P. 2013, *Nature*, 503, 500
 Luangtip, W., Roberts, T. P., Mineo, S., et al. 2014, arXiv:1410.1569
 Johnson, B. D., Schiminovich, D., Seibert, M., et al. 2007, *ApJS*, 173, 392
 Kaaret, P., Alonso-Herrero, A., Gallagher, J. S., et al. 2004, *MNRAS*, 348, L28
 Kalberla, P. M. W., Burton, W. B., Hartmann, D., et al. 2005, *A&A*, 440, 775
 Kaufman, M., Grupe, D., Elmegreen, B. G., et al. 2012, *AJ*, 144, 156
 Kennicutt, R. C., Jr. 1998, *ARA&A*, 36, 189
 Kennicutt, R. C., & Evans, N. J. 2012, *ARA&A*, 50, 531
 Konishi, M., Akiyama, M., Kajisawa, M., et al. 2011, *PASJ*, 63, 363
 Kubota, A., Mizuno, T., Makishima, K., et al. 2001, *ApJ*, 547, L119
 Kunth, D., & Oumlstlin, G. 2000, *A&A Rev.*, 10, 1
 Madhusudhan, N., Rappaport, S., Podsiadlowski, P., & Nelson, L. 2008, *ApJ*, 688, 1235
 Mapelli, M., Ripamonti, E., Zampieri, L., Colpi, M., & Bressan, A. 2010, *MNRAS*, 408, 234
 Mineo, S., Gilfanov, M., & Sunyaev, R. 2012a, *MNRAS*, 419, 2095
 Mineo, S., Gilfanov, M., & Sunyaev, R. 2012b, *MNRAS*, 426, 1870
 Mineo, S., Rappaport, S., Steinhorn, B., et al. 2013, *ApJ*, 771, 133
 Owen, R. A., Warwick R. S., 2009, *MNRAS*, 394, 1741
 Patrone, A., & Zampieri, L. 2008, *MNRAS*, 386, 543
 Pintore, F., Zampieri, L., Wolter, A., & Belloni, T. 2014, *MNRAS*, 439, 3461
 Podsiadlowski, P., Hsu, J. J. L., Joss, P. C., & Ross, R. R. 1993, *Nature*, 364, 509
 Pooley, D., Immler, S., & Filippenko, A. V. 2007, *The Astronomer's Telegram*, 1023, 1
 Pooley, D., & Lewin, W. H. G. 2004, *IAU Circ.*, 8323, 2
 Prestwich, A. H., Tsantaki, M., Zezas, A., et al. 2013, *ApJ*, 769, 92
 Roberts, T. P., Goad, M. R., Ward, M. J., et al. 2001, *MNRAS*, 325, L7
 Rupke, D. S. N., Kewley, L. J., & Chien, L.-H. 2010, *ApJ*, 723, 1255
 Sazonov, S., Krivonos, R., Revnivtsev, M., Churazov, E., & Sunyaev, R. 2008, *A&A*, 482, 517
 Smith, B. J., Struck, C., & Nowak, M. A. 2005, *AJ*, 129, 1350
 Smith, B. J., Swartz, D. A., Miller, O., et al. 2012, *AJ*, 143, 144
 Smith, B. J., Soria, R., Struck, C., et al. 2014, *AJ*, 147, 60
 Soria, R., Cropper, M., Pakull, M., Mushotzky, R., & Wu, K. 2005, *MNRAS*, 356, 12
 Soria, R., Risaliti, G., Elvis, M., et al. 2009, *ApJ*, 695, 1614
 Strickland, D. K., Heckman, T. M., Weaver, K. A., & Dahlem, M. 2000, *AJ*, 120, 2965
 Strickland, D. K., Heckman, T. M., Colbert, E. J. M., Hoopes, C. G., & Weaver, K. A. 2004, *ApJS*, 151, 193
 Struck, C. 1997, *ApJS*, 113, 269
 Struck, C., Kaufman, M., Brinks, E., et al. 2005, *MNRAS*, 364, 69
 Swartz, D. A., Ghosh, K. K., Tennant, A. F., & Wu, K. 2004, *ApJS*, 154, 519
 Swartz, D. A., Tennant, A. F., & Soria, R. 2009, *ApJ*, 703, 159
 Swartz, D. A., Soria, R., Tennant, A. F., & Yukita, M. 2011, *ApJ*, 741, 49
 Tüllmann, R., Pietsch, W., Rossa, J., Breitschwerdt, D., & Dettmar, R.-J. 2006, *A&A*, 448, 43
 Voss, R., & Gilfanov, M. 2006, *A&A*, 447, 71
 Voss, R., Nielsen, M. T. B., Nelemans, G., Fraser, M., & Smartt, S. J. 2011, *MNRAS*, 418, L124

- de Vaucouleurs, G., de Vaucouleurs, A., Corwin, H. G., Jr., et al. 1991, Volume 1-3, XII, 2069 pp. 7 figs.. Springer-Verlag Berlin Heidelberg New York,
- Walton, D. J., Roberts, T. P., Mateos, S., & Heard, V. 2011, MNRAS, 416, 1844
- Webb, N. A., Cseh, D., & Kirsten, F. 2014, Publications of the Astronomical Society of Australia, 31, 9
- Whitmore, B. C., & Schweizer, F. 1995, AJ, 109, 960
- Wolter, A., Trinchieri, G., & Colpi, M. 2006, MNRAS, 373, 1627
- Woosley, S. E., & Heger, A. 2012, ApJ, 752, 32
- Yukita, M., Swartz, D. A., Tennant, A. F., Soria, R., & Irwin, J. A. 2012, ApJ, 758, 105
- Zacharias, N., Monet, D. G., Levine, S. E., et al. 2004, Bulletin of the American Astronomical Society, 36, 1418
- Zezas, A., & Fabbiano, G. 2002, ApJ, 577, 726

TABLE A1
NGC2207/IC2163: X-RAY SOURCE PROPERTIES FOR ObsID 11228

Source	α_{J2000}	δ_{J2000}	0.5 – 8 keV	Signif	0.5 – 2 keV	2 – 8 keV	HR	L_X	F_X
(1)	(2)	(3)	(4)	(5)	(6)	(7)	(8)	(9)	(10)
(deg)	(deg)	(cts)	(σ)	(cts)	(cts)			($10^{38} \text{ erg s}^{-1}$)	($10^{-14} \text{ erg cm}^{-2} \text{ s}^{-1}$)
1†	94.06612	-21.3673	5.8 ± 4.5	3.4	3.9 ± 4.1	1.8 ± 3	-0.37 ± 0.84	7.6 ± 5.9	0.40 ± 0.32
2	94.06617	-21.3757	92 ± 11	38	63 ± 9.5	29 ± 6.9	-0.36 ± 0.12	120 ± 15	6.45 ± 0.79
3	94.06938	-21.3743	22 ± 6.2	2.5	20 ± 9.9	2.1 ± 3	-0.81 ± 0.25	30 ± 8.5	1.59 ± 0.45
4	94.07004	-21.3726	6.5 ± 4	2.3	3.2 ± 3.2	3.2 ± 3.3	-0.02 ± 0.71	3.9 ± 5.3	0.48 ± 0.29
5	94.07046	-21.3527	28 ± 6.8	3.3	21 ± 6.5	7.4 ± 4.3	-0.48 ± 0.24	38 ± 9.1	2.02 ± 0.48
6	94.07048	-21.3758	20 ± 6	8.6	9.7 ± 4.5	11 ± 4.7	0.05 ± 0.32	28 ± 8.3	1.50 ± 0.44
7	94.07176	-21.3806	41 ± 8	1.6	32 ± 7.2	9 ± 4.6	-0.56 ± 0.19	24 ± 11	2.87 ± 0.57
8	94.07191	-21.3599	13 ± 5.7	7.8	11 ± 4.8	6.5 ± 4	-0.26 ± 0.35	23 ± 9.5	1.24 ± 0.40
9	94.07487	-21.3677	33 ± 5.3	7.4	27 ± 6.6	6.4 ± 3.9	-0.63 ± 0.21	26 ± 9.4	2.44 ± 0.53
10	94.07500	-21.3647	14 ± 4.1	3.3	8.4 ± 4.4	6.1 ± 4	-0.12 ± 0.40	20 ± 7.4	1.04 ± 0.39
11	94.07521	-21.3686	6.5 ± 4.1	3.3	4.3 ± 3.9	1.1 ± 2.7	-0.65 ± 0.70	9.0 ± 5.5	0.48 ± 0.30
12	94.07536	-21.3707	5.1 ± 3.7	1.3	4.3 ± 3.5	0.94 ± 2.5	-0.63 ± 0.84	7.7 ± 5.5	0.41 ± 0.29
13	94.07818	-21.3743	25 ± 6.4	1.1	16 ± 5.4	3.6 ± 4.3	-0.30 ± 0.28	33 ± 8.5	1.74 ± 0.46
14	94.08054	-21.3641	13 ± 5.5	5.9	16 ± 5.4	3.6 ± 4.3	-0.66 ± 0.39	33 ± 8.5	0.91 ± 0.35
15	94.08430	-21.3851	18 ± 5.7	7.5	13 ± 5	5.4 ± 3.7	-0.41 ± 0.33	25 ± 6.6	1.31 ± 0.41
16	94.08525	-21.3740	5.8 ± 3.9	2.5	1.7 ± 2.9	3.4 ± 3.5	0.40 ± 0.79	7.8 ± 5.3	0.42 ± 0.28
17	94.08544	-21.3697	2.7 ± 6.7	1.5	20 ± 6	4.6 ± 4.3	-0.51 ± 0.25	36 ± 9	1.92 ± 0.48
18	94.08567	-21.3720	7.3 ± 4.1	2.9	4.2 ± 3.5	3.1 ± 3.2	-0.15 ± 0.64	9.8 ± 5.5	0.52 ± 0.30
19	94.08604	-21.3736	5.1 ± 3.8	2.1	5.6 ± 3.6	0 ± 2.1	-1.00 ± 0.74	6.9 ± 5.2	0.37 ± 0.28
20†	94.09177	-21.3727	70 ± 10	24	8.4 ± 4.8	61 ± 9.4	0.76 ± 0.12	95 ± 14	5.05 ± 0.74
21	94.09430	-21.3608	24 ± 6.6	11	17 ± 5.7	7 ± 4.3	-0.43 ± 0.28	33 ± 8.9	1.77 ± 0.45
22	94.09828	-21.3707	1.7 ± 4.3	3.3	5.7 ± 3.9	2 ± 2.9	-0.47 ± 0.62	11 ± 5.9	0.57 ± 0.32
23	94.10083	-21.3866	7.6 ± 4.1	3.4	7.6 ± 4.1	0 ± 2	-1.00 ± 0.53	13 ± 7	0.69 ± 0.37
24	94.10100	-21.3627	9.7 ± 4.6	3.9	5.2 ± 3.6	4.3 ± 3.6	-0.08 ± 0.54	13 ± 6.4	0.71 ± 0.34
25	94.10377	-21.3641	6.4 ± 3.9	3.6	4.3 ± 3.3	2.2 ± 2.9	-0.32 ± 0.71	8.9 ± 5.5	0.47 ± 0.29
26	94.10472	-21.3749	13 ± 5.3	3.9	7.3 ± 4.3	6.2 ± 4.1	-0.08 ± 0.44	19 ± 7.5	1.02 ± 0.40
27	94.10630	-21.3704	6.4 ± 4	2.6	0 ± 2.1	6.7 ± 4	1.00 ± 0.63	9.3 ± 5.8	0.49 ± 0.31
28	94.10824	-21.3771	14 ± 5.1	5.2	6.5 ± 3.9	7.4 ± 4.1	0.07 ± 0.41	22 ± 8	1.17 ± 0.43
29	94.11017	-21.3701	7.8 ± 4.3	5.2	6.8 ± 4.2	0.95 ± 2.6	-0.75 ± 0.59	11 ± 6.3	0.60 ± 0.34
30	94.11180	-21.3697	13 ± 5	5.2	12 ± 4.8	1.1 ± 2.5	-0.83 ± 0.37	22 ± 8.5	1.17 ± 0.45
31	94.11419	-21.3712	5.4 ± 3.7	2	4.3 ± 3.5	1.1 ± 2.5	-0.60 ± 0.79	9.1 ± 6.2	0.49 ± 0.33
32	94.11818	-21.3609	15 ± 3.3	7.2	11 ± 4.7	4.4 ± 3.5	-0.42 ± 0.37	24 ± 8.5	1.30 ± 0.46
33	94.12197	-21.3680	5.5 ± 3.8	2	5.5 ± 3.8	0 ± 2.1	-1.00 ± 0.75	8.1 ± 5.5	0.43 ± 0.29
34	94.12488	-21.3740	15 ± 5.5	8.3	11 ± 4.9	4.1 ± 3.5	-0.45 ± 0.38	21 ± 7.9	1.14 ± 0.42

NOTE. — (1) Source number, (2) Right Ascension (RA), (3) Declination (Dec), (4) Net counts in broad (0.5–8 keV) band. The uncertainty expressed here takes into account the fluctuations in the source as well as in the background. (5) Broad band source detection significance from *wavdetect*. This computes how unlikely it is for the background in the customized psf region to fluctuate to yield the detected number of counts. Note that the psf region is optimized differently in *wavdetect* than in the calculation of column (4) and is typically larger than in the latter. (6)-(7) Net counts in soft (0.5–2 keV) and hard (2–8 keV) bands respectively. Uncertainties in net counts are quoted to 1 σ . (7) Hardness ratio, computed with eq. (1). Uncertainties were obtained by applying error propagation to the uncertainties in the net counts. (8) X-ray luminosity in the 0.5–8 keV band, (9) X-ray flux in the 0.5–8 keV band. † Central Active Galactic Nucleus, ‡ Extended soft X-ray source.

APPENDIX

A. SOURCE LISTS FOR ALL INDIVIDUAL AND COMBINED OBSERVATIONS

TABLE A2
NGC2207/IC2163: X-RAY SOURCE PROPERTIES FOR OBSID 14914

Source	α_{J2000}	δ_{J2000}	0.5 – 8 keV	Signif	0.5 – 2 keV	2 – 8 keV	HR	L_X	F_X
	(deg)	(deg)	(cts)	(σ)	(cts)	(cts)		($10^{38} \text{ erg s}^{-1}$)	($10^{-14} \text{ erg cm}^{-2} \text{ s}^{-1}$)
(1)	(2)	(3)	(4)	(5)	(6)	(7)	(8)	(9)	(10)
1	94.05535	-21.3669	7.8 \pm 4.3	3.2	7.8 \pm 4.3	0 \pm 2.1	-1.00 \pm 0.54	7 \pm 3.9	0.37 \pm 0.21
2†	94.06608	-21.3677	18 \pm 6.1	8.3	12 \pm 5.2	6.3 \pm 4	-0.30 \pm 0.35	16 \pm 5.3	0.85 \pm 0.28
3‡	94.06618	-21.3757	130 \pm 13	45	89 \pm 11	46 \pm 8.2	-0.32 \pm 0.20	120 \pm 12	6.26 \pm 0.62
4	94.06938	-21.3743	38 \pm 7.7	15	28 \pm 6.8	9.6 \pm 4.3	-0.49 \pm 0.30	33 \pm 6.7	1.76 \pm 0.36
5	94.07044	-21.3522	46 \pm 5.5	6.4	33 \pm 4.4	7.4 \pm 4.2	-0.06 \pm 0.38	14 \pm 4.8	0.73 \pm 0.35
6	94.07048	-21.3522	46 \pm 5.5	6.4	33 \pm 4.4	7.4 \pm 4.2	-0.44 \pm 0.18	40 \pm 7.3	2.14 \pm 0.39
7	94.07074	-21.3809	8.3 \pm 4.4	3.5	5.3 \pm 3.8	3.1 \pm 3.3	-0.27 \pm 0.60	7.3 \pm 3.9	0.39 \pm 0.21
8	94.07178	-21.3806	6.8 \pm 4.4	2.6	4.2 \pm 3.8	2.6 \pm 3.6	-0.33 \pm 0.15	5.9 \pm 8.6	3.15 \pm 0.46
9	94.07187	-21.3529	1.2 \pm 3.3	6.1	9.9 \pm 4.6	4.4 \pm 3.5	-0.35 \pm 0.39	12 \pm 4.5	0.66 \pm 0.24
10	94.07493	-21.3678	1.9 \pm 5.7	8.6	9.7 \pm 5.6	8.1 \pm 4.5	-0.04 \pm 0.33	27 \pm 5.8	0.48 \pm 0.34
11	94.07502	-21.3647	9.6 \pm 4.5	4.3	6.4 \pm 3.5	3.3 \pm 3.3	-0.32 \pm 0.33	8.3 \pm 3.9	0.44 \pm 0.21
12	94.07529	-21.3743	9.6 \pm 4.5	4.3	19 \pm 5.8	11 \pm 4.7	-0.39 \pm 0.24	26 \pm 3.7	0.38 \pm 0.32
13	94.08011	-21.3827	7.9 \pm 4.1	3.4	8.0 \pm 4.4	7.6 \pm 4.1	1.00 \pm 0.54	6.8 \pm 3.7	0.36 \pm 0.20
14	94.08054	-21.3642	8.4 \pm 4.6	4	8.4 \pm 3.4	0.96 \pm 2.6	-0.80 \pm 0.51	7.9 \pm 4	0.42 \pm 0.21
15	94.08268	-21.3629	23 \pm 6.3	3.6	12 \pm 3.5	4.2 \pm 3.5	-0.02 \pm 0.57	8 \pm 4	0.42 \pm 0.21
16	94.08540	-21.3697	13 \pm 6.3	5.2	13 \pm 4.8	1.1 \pm 2.6	0.00 \pm 0.39	21 \pm 5.6	1.10 \pm 0.30
17	94.08613	-21.3737	14 \pm 6.3	5.2	13 \pm 4.8	1.1 \pm 2.6	-0.84 \pm 0.35	12 \pm 4.6	0.63 \pm 0.34
18	94.08674	-21.3708	9.3 \pm 4.6	3.6	26 \pm 6.5	13 \pm 5	-0.33 \pm 0.30	33 \pm 6.6	1.77 \pm 0.35
19	94.08898	-21.3738	9.3 \pm 4.6	3.6	6.2 \pm 4	3.2 \pm 3.2	-0.32 \pm 0.54	8 \pm 3.9	0.43 \pm 0.21
20†	94.09175	-21.3727	86 \pm 11	30	19 \pm 6.4	68 \pm 9.9	0.56 \pm 0.13	74 \pm 9.7	3.94 \pm 0.52
21‡	94.09426	-21.3609	31 \pm 7.1	13	22 \pm 6.2	8.7 \pm 4.4	-0.43 \pm 0.24	26 \pm 6.1	1.41 \pm 0.32
22	94.09786	-21.3719	33 \pm 7.7	15	22 \pm 6.1	17 \pm 5.5	-0.12 \pm 0.31	34 \pm 6.6	1.80 \pm 0.35
23	94.09819	-21.3708	6.2 \pm 4.1	8	12 \pm 5	9.8 \pm 4.7	-0.10 \pm 0.31	19 \pm 5.4	0.99 \pm 0.29
24	94.09921	-21.3710	6.7 \pm 4.1	8	6.9 \pm 4.1	5.0 \pm 3.8	1.00 \pm 0.59	5.8 \pm 3.6	0.31 \pm 0.19
25	94.10011	-21.3697	7.5 \pm 4.2	3.2	2 \pm 3.1	5.6 \pm 3.8	0.48 \pm 0.64	6.5 \pm 3.7	0.35 \pm 0.19
26	94.10093	-21.3627	13 \pm 5.7	7.3	14 \pm 5.1	4.2 \pm 3.3	-0.53 \pm 0.33	15 \pm 4.9	0.82 \pm 0.26
27	94.10493	-21.3749	13 \pm 5.7	5.5	5.4 \pm 3.8	7.5 \pm 3.3	0.16 \pm 0.44	11 \pm 4.4	0.59 \pm 0.23
28	94.10608	-21.3733	10 \pm 4.7	4.4	7.2 \pm 4.1	3.3 \pm 3.3	-0.38 \pm 0.49	9 \pm 4.7	0.48 \pm 0.21
29*	94.10819	-21.3771	1.5 \pm 5.5	7.1	11 \pm 4.8	4.4 \pm 3.6	-0.42 \pm 0.38	13 \pm 4.7	0.70 \pm 0.25
30	94.10869	-21.3750	7.3 \pm 4.1	3.2	3 \pm 3.2	4.4 \pm 3.5	0.18 \pm 0.64	6.4 \pm 3.6	0.34 \pm 0.19
31	94.10971	-21.3701	12 \pm 5.2	6.3	8 \pm 4.3	4.2 \pm 3.5	-0.33 \pm 0.44	10 \pm 4.3	0.58 \pm 0.23
32	94.11052	-21.3701	33 \pm 7.2	13	19 \pm 5.8	14 \pm 5.3	-0.16 \pm 0.23	29 \pm 6.4	1.93 \pm 0.33
33	94.11171	-21.3698	33 \pm 7.2	13	19 \pm 5.8	14 \pm 5.3	-0.13 \pm 0.23	29 \pm 6.4	1.93 \pm 0.33
34	94.11250	-21.3632	4.9 \pm 3.8	2.3	1.5 \pm 3.2	3.3 \pm 3.3	-0.34 \pm 0.29	20 \pm 5.4	1.04 \pm 0.29
35	94.11316	-21.3783	4.9 \pm 3.8	2.3	1.5 \pm 3.2	3.3 \pm 3.3	0.34 \pm 0.92	4.4 \pm 3.3	0.23 \pm 0.18
36	94.11416	-21.3713	6.3 \pm 4	2.3	5.2 \pm 3.7	0.96 \pm 2.6	-0.65 \pm 0.70	5.5 \pm 3.5	0.30 \pm 0.21
37	94.11693	-21.3793	6.5 \pm 4	2.3	5.5 \pm 3.8	0.96 \pm 2.6	-0.71 \pm 0.70	8.5 \pm 4	0.35 \pm 0.21
38	94.11809	-21.3609	34 \pm 7.3	14	20 \pm 5.9	14 \pm 5.3	-0.17 \pm 0.23	29 \pm 6.4	1.96 \pm 0.34
39	94.11911	-21.3741	28 \pm 6.4	13	19 \pm 5.8	14 \pm 5.3	0.49 \pm 0.13	28 \pm 6.4	1.93 \pm 0.33

NOTE. — (1) Source number, (2) Right Ascension (RA), (3) Declination (Dec), (4) Net counts in broad (0.5–8 keV) band. The uncertainty expressed here takes into account the fluctuations in the source as well as in the background. (5) Broad band source detection significance from *wavdetect*. This computes how unlikely it is for the background in the customized psf region to fluctuate to yield the detected number of counts. Note that the psf region is optimized differently in *wavdetect* than in the calculation of column (4) and is typically larger than in the latter. (6)–(7) Net counts in soft (0.5–2 keV) and hard (2–8 keV) bands respectively. Uncertainties in net counts are quoted to 1σ . (7) Hardness ratio, computed with eq. (1). Uncertainties were obtained by applying error propagation to the uncertainties in the net counts. (8) X-ray luminosity in the 0.5–8 keV band, (9) X-ray flux in the 0.5–8 keV band. † Central Active Galactic Nucleus, ‡ Extended soft X-ray source, * SN 2003H (3.1'' match).

TABLE A3
NGC2207/IC2163: X-RAY SOURCE PROPERTIES FOR OBSID 14799

Source	α_{J2000}	δ_{J2000}	0.5 – 8 keV	Signif	0.5 – 2 keV	2 – 8 keV	HR	L_X	F_X
	(deg)	(deg)	(cts)	(σ)	(cts)	(cts)		($10^{38} \text{ erg s}^{-1}$)	($10^{-14} \text{ erg cm}^{-2} \text{ s}^{-1}$)
(1)	(2)	(3)	(4)	(5)	(6)	(7)	(8)	(9)	(10)
1	94.05536	-21.3669	6.5 \pm 4	3	4.4 \pm 3.5	2.1 \pm 3	-0.36 \pm 0.71	11 \pm 6.9	0.60 \pm 0.37
2	94.06615	-21.3757	31 \pm 7	14	22 \pm 6.1	8.8 \pm 4.4	-0.43 \pm 0.23	54 \pm 12	2.87 \pm 0.66
3†	94.06619	-21.3676	8 \pm 4.4	3.7	4.7 \pm 3.8	3.3 \pm 3.2	-0.17 \pm 0.62	15 \pm 8.3	0.81 \pm 0.44
4	94.06937	-21.3742	12 \pm 4.9	5.1	5.5 \pm 3.7	6.2 \pm 4	0.06 \pm 0.47	20 \pm 8.5	1.08 \pm 0.45
5	94.07055	-21.3527	33 \pm 7.3	15	24 \pm 6.4	8.7 \pm 4.4	-0.47 \pm 0.22	59 \pm 13	3.12 \pm 0.69
6	94.07061	-21.3598	5.1 \pm 3.8	2.4	4.4 \pm 3.5	0.66 \pm 2.6	-0.74 \pm 0.91	8.8 \pm 6.5	0.47 \pm 0.35
7	94.07176	-21.3806	5.3 \pm 3.8	2.2	3.1 \pm 2.1	2.2 \pm 1.6	-0.18 \pm 0.18	92 \pm 15	4.89 \pm 0.82
8	94.07309	-21.3786	8.2 \pm 4.4	3.9	7.4 \pm 4.2	0.82 \pm 2.6	-0.80 \pm 0.57	14 \pm 7.6	0.76 \pm 0.40
9	94.07486	-21.3679	13 \pm 5	5.7	9.6 \pm 4.5	3.3 \pm 3.2	-0.49 \pm 0.41	23 \pm 9	1.24 \pm 0.48
10	94.07502	-21.3647	12 \pm 4.8	5.4	7.3 \pm 4.1	3.2 \pm 3.2	-0.27 \pm 0.46	20 \pm 8.4	1.06 \pm 0.45
11	94.07530	-21.3686	11 \pm 4.7	4.9	7.6 \pm 4.1	3.3 \pm 3.2	-0.40 \pm 0.47	20 \pm 8.5	1.05 \pm 0.45
12	94.07536	-21.3708	12 \pm 4.9	5.9	5.4 \pm 3.8	6.6 \pm 4	0.09 \pm 0.46	21 \pm 8.5	1.10 \pm 0.45
13*	94.07653	-21.3758	36 \pm 7.7	18	5.4 \pm 3.8	31 \pm 7.2	0.70 \pm 0.19	63 \pm 13	3.34 \pm 0.71
14	94.07819	-21.3743	22 \pm 6.2	11	12 \pm 4.8	11 \pm 4.7	-0.04 \pm 0.30	39 \pm 11	2.05 \pm 0.57
15	94.08047	-21.3642	9.9 \pm 4.7	5.3	8.7 \pm 4.5	1.1 \pm 2.6	-0.77 \pm 0.48	17 \pm 8.1	0.91 \pm 0.43
16	94.08548	-21.3697	8.8 \pm 4.4	4.4	6.7 \pm 4	2.1 \pm 3	-0.52 \pm 0.56	16 \pm 8	0.85 \pm 0.43
17	94.08617	-21.3776	4.2 \pm 3.5	2	1.1 \pm 2.5	3.1 \pm 3.2	0.48 \pm 0.98	7.3 \pm 6	0.39 \pm 0.32
18	94.08675	-21.3809	13 \pm 5.2	6.5	5.6 \pm 3.8	3.8 \pm 4.3	0.16 \pm 0.43	23 \pm 8.9	1.24 \pm 0.48
19	94.08907	-21.3738	4.2 \pm 3.5	1.9	2 \pm 2.9	2.2 \pm 2.9	0.03 \pm 0.98	4.2 \pm 6	0.39 \pm 0.32
20†	94.09177	-21.3728	39 \pm 8	16	8.9 \pm 4.6	30 \pm 7.1	0.55 \pm 0.20	70 \pm 14	3.74 \pm 0.76
21‡	94.09791	-21.3719	28 \pm 6.8	11	15 \pm 5.4	12 \pm 4.9	-0.12 \pm 0.26	50 \pm 12	2.67 \pm 0.65
22	94.10066	-21.3865	12 \pm 4.9	5.5	6.6 \pm 3.9	5.5 \pm 3.7	-0.09 \pm 0.45	21 \pm 8.4	1.11 \pm 0.45
23	94.10100	-21.3627	6.4 \pm 4	2.6	4.3 \pm 3.5	2.1 \pm 3	-0.35 \pm 0.72	7 \pm 6.3	0.60 \pm 0.37
24	94.10381	-21.3639	4 \pm 3.6	1.7	0 \pm 2.1	4.5 \pm 3.6	1.00 \pm 0.94	11 \pm 6.3	0.37 \pm 0.34
25	94.10484	-21.3748	8.9 \pm 4.6	3.5	6.1 \pm 4	2.9 \pm 3.3	-0.35 \pm 0.57	17 \pm 8.8	0.93 \pm 0.47
26	94.10820	-21.3771	7.7 \pm 4.3	3.4	5.5 \pm 3.9	2.1 \pm 3	-0.44 \pm 0.63	13 \pm 9.4	0.71 \pm 0.40
27	94.11050	-21.3702	15 \pm 5.4	6.7	9.2 \pm 4.5	6.2 \pm 3.9	-0.19 \pm 0.38	27 \pm 9.4	1.44 \pm 0.50
28	94.11194	-21.3698	10 \pm 4.7	5.3	6.2 \pm 3.9	4.2 \pm 3.5	-0.19 \pm 0.50	18 \pm 8.1	0.97 \pm 0.43
29	94.11255	-21.3631	5.4 \pm 3.7	2.4	3.3 \pm 3.2	2.2 \pm 1.6	-0.20 \pm 0.80	9.5 \pm 6.5	0.51 \pm 0.35
30	94.11814	-21.3609	8.8 \pm 4.4	3.7	5.5 \pm 3.7	3.3 \pm 3.2	-0.25 \pm 0.56	15 \pm 7.7	0.83 \pm 0.41
31	94.12123	-21.3808	3.9 \pm 3.6	2.3	4.2 \pm 3.6	0 \pm 2.1	-1.00 \pm 1.01	6.7 \pm 6.2	0.36 \pm 0.33

TABLE A4
NGC2207/IC2163: X-RAY SOURCE PROPERTIES FOR ObsID 14915

Source	α_{J2000} (deg)	δ_{J2000} (deg)	0.5 – 8 keV (cts)	Signif (σ)	0.5 – 2 keV (cts)	2 – 8 keV (cts)	HR	L_X (10^{38} erg s $^{-1}$)	F_X (10^{-14} erg cm $^{-2}$ s $^{-1}$)
(1)	(2)	(3)	(4)	(5)	(6)	(7)	(8)	(9)	(10)
1	94.05543	-21.3669	5.6 \pm 3.8	2.3	4.5 \pm 3.6	1.1 \pm 2.6	-0.60 \pm 0.79	4.9 \pm 3.3	0.26 \pm 0.18
2†	94.06613	-21.3675	20 \pm 6.3	11	10 \pm 5	9.8 \pm 4.6	-0.01 \pm 0.34	17 \pm 5.4	0.91 \pm 0.29
3†	94.06623	-21.3757	39 \pm 7.9	16	27 \pm 6.7	12 \pm 5	-0.38 \pm 0.21	33 \pm 6.7	1.78 \pm 0.36
4	94.06792	-21.3723	12 \pm 5	4.5	7.7 \pm 4.2	4.2 \pm 3.6	-0.29 \pm 0.46	10 \pm 4.3	0.54 \pm 0.23
5	94.06939	-21.3743	23 \pm 6.3	8	13 \pm 5.1	10 \pm 4.6	-0.11 \pm 0.30	19 \pm 5.4	1.03 \pm 0.23
6	94.06973	-21.3766	9.3 \pm 4.6	4	8.4 \pm 4.4	0.95 \pm 2.6	-0.80 \pm 0.51	8 \pm 3.9	0.42 \pm 0.21
7	94.07042	-21.3753	6.2 \pm 4	2.7	3 \pm 3.3	3.2 \pm 3.3	0.02 \pm 0.74	5.3 \pm 3.4	0.28 \pm 0.18
8	94.07057	-21.3527	13 \pm 5.2	6	3.2 \pm 3.3	10 \pm 4.6	0.52 \pm 0.41	23 \pm 9	1.24 \pm 0.48
9	94.07180	-21.3827	41 \pm 8	17	29 \pm 6.9	12 \pm 5	-0.43 \pm 0.20	35 \pm 6.9	1.89 \pm 0.37
10	94.07292	-21.3720	5.8 \pm 3.3	2.6	3.7 \pm 3.3	2.5 \pm 2.9	-0.28 \pm 0.38	5 \pm 3.4	0.28 \pm 0.18
11	94.07498	-21.3678	15 \pm 4	6	11 \pm 4.6	4.5 \pm 3.5	-0.44 \pm 0.39	13 \pm 4.4	0.69 \pm 0.24
12	94.07507	-21.3646	23 \pm 6.2	10	16 \pm 4.6	6.7 \pm 3.5	-0.54 \pm 0.39	20 \pm 5.5	1.06 \pm 0.29
13	94.07534	-21.3686	14 \pm 5.2	6.1	10 \pm 4.2	3.1 \pm 2.2	-0.54 \pm 0.40	12 \pm 4.4	0.62 \pm 0.24
14	94.07819	-21.3743	54 \pm 9.9	23	37 \pm 4.2	17 \pm 3.6	-0.37 \pm 0.17	46 \pm 4.6	2.47 \pm 0.41
15	94.08049	-21.3642	14 \pm 5.1	7.2	10 \pm 4.2	4.3 \pm 3.5	-0.40 \pm 0.39	12 \pm 4.4	0.66 \pm 0.24
16	94.08225	-21.3784	6.3 \pm 4.1	3.2	1.8 \pm 3.3	4.2 \pm 3.6	0.42 \pm 0.75	5.4 \pm 3.5	0.29 \pm 0.19
17	94.08265	-21.3728	11 \pm 4.8	5.7	8 \pm 3.3	4.2 \pm 3.6	-0.67 \pm 0.48	9 \pm 4.2	0.48 \pm 0.22
18	94.08532	-21.3740	13 \pm 5.1	5.3	2.5 \pm 3.3	9.7 \pm 3.6	0.50 \pm 0.42	11 \pm 4.4	0.59 \pm 0.24
19	94.08578	-21.3697	12 \pm 5	5.3	2.5 \pm 3.3	3.2 \pm 3.3	-0.46 \pm 0.45	10 \pm 4.3	0.55 \pm 0.23
20	94.08675	-21.3808	25 \pm 6.4	11	2.1 \pm 3.3	3.1 \pm 3.3	-0.67 \pm 0.25	21 \pm 5.5	1.13 \pm 0.29
21	94.08708	-21.3711	8.6 \pm 4.5	4.2	5.5 \pm 3.6	3.1 \pm 3.3	-0.28 \pm 0.59	7.4 \pm 3.8	0.39 \pm 0.20
22†	94.09180	-21.3727	160 \pm 15	51	13 \pm 5.6	150 \pm 14	0.83 \pm 0.07	140 \pm 13	7.31 \pm 0.68
23	94.09431	-21.3608	8.7 \pm 4.4	4.7	6.4 \pm 4	2.2 \pm 3	-0.49 \pm 0.56	7.5 \pm 3.9	0.40 \pm 0.21
24	94.09820	-21.3709	22 \pm 6.2	9.1	14 \pm 5.1	8.1 \pm 4.3	-0.25 \pm 0.30	19 \pm 5.3	1.00 \pm 0.23
25	94.10011	-21.3696	7.6 \pm 4.2	3.1	3.1 \pm 3.3	4.5 \pm 3.5	0.18 \pm 0.65	6.6 \pm 3.7	0.35 \pm 0.20
26	94.10064	-21.3812	7.1 \pm 4.1	3.4	2.8 \pm 3.3	4.2 \pm 3.5	0.19 \pm 0.67	6.5 \pm 3.8	0.35 \pm 0.20
27	94.10071	-21.3862	22 \pm 6.2	9.7	20 \pm 6	2.2 \pm 3	-0.80 \pm 0.25	19 \pm 5.4	1.02 \pm 0.23
28	94.10097	-21.3627	10 \pm 4.7	4.4	9.1 \pm 4.5	1.1 \pm 2.3	-0.79 \pm 0.45	8.9 \pm 4.1	0.47 \pm 0.22
29	94.10385	-21.3640	2.5 \pm 3.5	6.4	9.6 \pm 4.5	5.3 \pm 3.7	-0.29 \pm 0.39	13 \pm 4.6	0.69 \pm 0.24
30	94.10485	-21.3748	2.5 \pm 3.5	10	14 \pm 5.2	1.4 \pm 2.8	-0.12 \pm 0.78	21 \pm 5.6	1.14 \pm 0.30
31	94.10568	-21.3770	2.4 \pm 3.7	3.5	5.4 \pm 3.7	0 \pm 2.1	-1.00 \pm 0.75	4.3 \pm 3.3	0.26 \pm 0.18
32	94.10633	-21.3703	6.3 \pm 4.1	3.3	0.8 \pm 3.3	6.5 \pm 3.9	0.78 \pm 0.63	6.3 \pm 3.3	0.34 \pm 0.19
33	94.10823	-21.3770	6.2 \pm 4.1	3.3	4.1 \pm 3.3	2.1 \pm 3.4	-0.32 \pm 0.75	3.6 \pm 3.6	0.30 \pm 0.19
34	94.11048	-21.3701	70 \pm 9.9	29	45 \pm 6.6	25 \pm 6.4	-0.29 \pm 0.13	60 \pm 6.6	3.20 \pm 0.46
35	94.11177	-21.3698	3.5 \pm 2.9	14	2.5 \pm 3.3	10 \pm 4.6	-0.42 \pm 0.28	30 \pm 6.5	1.60 \pm 0.35
36	94.11363	-21.3733	4.2 \pm 3.6	2.1	3.1 \pm 3.3	1.1 \pm 2.6	-0.47 \pm 1.00	2.8 \pm 3.2	0.20 \pm 0.17
37	94.11431	-21.3713	9.1 \pm 4.5	4	7.3 \pm 4.1	5.3 \pm 3.6	-0.61 \pm 0.53	7.8 \pm 3.9	0.42 \pm 0.21
38	94.11816	-21.3609	23 \pm 6.2	9.5	18 \pm 5.6	0.2 \pm 3.6	-0.54 \pm 0.28	20 \pm 5.4	1.06 \pm 0.29
39	94.12033	-21.3768	7 \pm 4.2	3.2	6.2 \pm 4	0.83 \pm 2.6	-0.76 \pm 0.66	6.1 \pm 3.6	0.32 \pm 0.19
40	94.12192	-21.3680	19 \pm 5.8	8.7	18 \pm 5.7	0.95 \pm 2.5	-0.90 \pm 0.25	17 \pm 5	0.88 \pm 0.27
41	94.12480	-21.3786	6.5 \pm 4	8.7	4.3 \pm 3.9	2.2 \pm 2.9	-0.32 \pm 0.70	5.7 \pm 3.5	0.30 \pm 0.19

NOTE. — (1) Source number, (2) Right Ascension (RA), (3) Declination (Dec), (4) Net counts in broad (0.5–8 keV) band. The uncertainty expressed here takes into account the fluctuations in the source as well as in the background. (5) Broad band source detection significance from *wavdetect*. This computes how unlikely it is for the background in the customized psf region to fluctuate to yield the detected number of counts. Note that the psf region is optimized differently in *wavdetect* than in the calculation of column (4) and is typically larger than in the latter. (6)-(7) Net counts in soft (0.5–2 keV) and hard (2–8 keV) bands respectively. Uncertainties in net counts are quoted to 1 σ . (7) Hardness ratio, computed with eq. (1). Uncertainties were obtained by applying error propagation to the uncertainties in the net counts. (8) X-ray luminosity in the 0.5–8 keV band, (9) X-ray flux in the 0.5–8 keV band. † Central Active Galactic Nucleus, ‡ Extended soft X-ray source.

TABLE A5
NGC2207/IC2163: X-RAY SOURCE PROPERTIES FOR THE COMBINED IMAGE

Source	α_{J2000} (deg)	δ_{J2000} (deg)	0.5–8 keV (cts)	Signif (σ)	0.5–2 keV (cts)	2–8 keV (cts)	HR	L_X (10^{38} erg s $^{-1}$)	F_X (10^{-14} erg cm $^{-2}$ s $^{-1}$)
(1)	(2)	(3)	(4)	(5)	(6)	(7)	(8)	(9)	(10)
1	94.05537	-21.3669	22 ± 6.3	8.8	18 ± 5.7	4 ± 3.6	-0.64 ± 0.29	6 ± 1.7	0.32 ± 0.09
2	94.06618	-21.3757	300 ± 19	82	200 ± 16	95 ± 11	-0.36 ± 0.06	81 ± 5.3	4.32 ± 0.28
3†	94.06618	-21.3675	67 ± 10	19	43 ± 8.8	24 ± 6.4	-0.29 ± 0.15	19 ± 2.9	0.99 ± 0.15
4	94.06674	-21.3581	6.9 ± 4.4	3.3	6 ± 4	0.93 ± 3	-0.73 ± 0.76	2 ± 1.2	0.10 ± 0.07
5	94.06788	-21.3726	17 ± 6.1	3.4	11 ± 5.2	5.6 ± 4.1	-0.35 ± 0.39	4.6 ± 1.7	0.25 ± 0.09
6*	94.06856	-21.3692	15 ± 5.4	3.4	5.3 ± 4.6	5.2 ± 3.9	-0.01 ± 0.57	2.9 ± 1.7	0.15 ± 0.08
7	94.06937	-21.3743	95 ± 12	26	67 ± 10	28 ± 7	-0.41 ± 0.12	26 ± 3.2	1.40 ± 0.17
8	94.06969	-21.3766	14 ± 5.3	5	8.3 ± 5.2	1.3 ± 3.1	-0.81 ± 0.41	3.8 ± 1.2	0.20 ± 0.08
9	94.07010	-21.3726	18 ± 6.3	6.2	8.2 ± 4.7	10 ± 4.8	0.11 ± 0.37	5.1 ± 1.7	0.27 ± 0.09
10	94.07048	-21.3732	15 ± 5.1	14	26 ± 6.7	28 ± 6.3	-0.09 ± 0.19	15 ± 2.4	0.70 ± 0.13
11	94.07050	-21.3732	120 ± 13	45	86 ± 11	40 ± 9.9	-0.33 ± 0.11	41 ± 4.4	2.10 ± 0.23
12	94.07052	-21.3739	13 ± 5.3	4.5	8.6 ± 4.5	4.1 ± 3.9	-0.33 ± 0.47	3.5 ± 1.3	0.18 ± 0.08
13	94.07074	-21.3809	21 ± 6.2	7.3	10 ± 4.9	17 ± 5.9	0.02 ± 0.34	5.8 ± 1.3	0.31 ± 0.09
14	94.07177	-21.3807	210 ± 17	34	140 ± 14	74 ± 10	-0.30 ± 0.08	58 ± 4.8	3.09 ± 0.24
15	94.07189	-21.3999	21 ± 8.1	16	24 ± 6.5	17 ± 7	-0.17 ± 0.29	16 ± 2.3	0.61 ± 0.12
16	94.07299	-21.3724	7.9 ± 4.6	2.7	5.3 ± 6.4	2.6 ± 3.3	-0.37 ± 0.65	2.2 ± 3.0	0.12 ± 0.07
17	94.07301	-21.3787	23 ± 6.8	2.7	20 ± 9.3	3.3 ± 5.6	-0.72 ± 0.28	2.4 ± 1.3	0.34 ± 0.10
18	94.07493	-21.3743	85 ± 11	23	65 ± 9.3	30 ± 7	-0.19 ± 0.14	24 ± 3.5	1.1 ± 0.15
19	94.07506	-21.3687	75 ± 10	14	33 ± 9.3	10 ± 4.8	-0.49 ± 0.19	12 ± 2.3	0.61 ± 0.12
20	94.07536	-21.3708	20 ± 8.1	7.3	3.2 ± 5.1	3.9 ± 4.4	-0.21 ± 0.33	1.8 ± 1.3	0.20 ± 0.09
21	94.07548	-21.3738	41 ± 8.1	1.3	6.4 ± 3.2	3.9 ± 4.4	0.69 ± 0.18	5.6 ± 2.3	0.60 ± 0.12
22	94.07707	-21.3632	6.5 ± 4.2	2.8	3.9 ± 3.5	2.6 ± 3.4	-0.19 ± 0.15	1.8 ± 1.3	0.10 ± 0.06
23	94.07818	-21.3743	130 ± 13	42	85 ± 11	49 ± 6.3	-0.27 ± 0.10	37 ± 3.5	1.95 ± 0.20
24	94.08016	-21.3827	15 ± 5.5	6.4	0 ± 2.1	15 ± 3.6	1.00 ± 0.27	4.2 ± 1.5	0.22 ± 0.08
25	94.08054	-21.3642	49 ± 9.5	1.7	40 ± 8.1	8.7 ± 3.6	-0.64 ± 0.16	13 ± 2.3	0.77 ± 0.13
26	94.08208	-21.3620	14 ± 5.6	5.8	9.5 ± 4.6	4.8 ± 3.6	-0.32 ± 0.42	4 ± 1.5	0.21 ± 0.08
27	94.08222	-21.3784	15 ± 6.6	6.3	2.3 ± 3.4	1.3 ± 3.4	0.70 ± 0.38	4.3 ± 1.6	0.23 ± 0.08
28	94.08267	-21.3629	22 ± 6.4	9	16 ± 5.7	6.2 ± 4.4	-0.45 ± 0.29	6.3 ± 1.8	0.33 ± 0.10
29	94.08410	-21.3736	11 ± 4.9	3.5	5.9 ± 4.4	4.3 ± 3.3	-0.12 ± 0.52	2.9 ± 1.8	0.16 ± 0.07
30	94.08431	-21.3851	20 ± 6.3	5.2	1.2 ± 5.2	2.5 ± 3.3	-0.28 ± 0.33	2.6 ± 1.4	0.30 ± 0.09
31	94.08528	-21.3741	24 ± 6.8	2.4	9.2 ± 4.4	3.5 ± 3.6	0.21 ± 0.29	2.2 ± 2.6	0.36 ± 0.10
32	94.08544	-21.3697	71 ± 10	23	46 ± 8.4	25 ± 6.5	-0.31 ± 0.14	20 ± 2.6	1.05 ± 0.15
33	94.08568	-21.3719	11 ± 5.1	4	5.2 ± 4.4	5.8 ± 4.4	0.05 ± 0.52	3 ± 1.4	0.16 ± 0.07
34	94.08611	-21.3737	24 ± 6.5	7.1	23 ± 6.4	0.63 ± 2.6	-0.95 ± 0.21	6.5 ± 1.8	0.34 ± 0.09
35	94.08616	-21.3776	9.6 ± 4.8	3.4	4.8 ± 3.6	4.9 ± 3.6	0.03 ± 0.56	2.6 ± 1.3	0.14 ± 0.07
36	94.08675	-21.3808	77 ± 10	28	32 ± 8.7	25 ± 6.3	-0.34 ± 0.14	21 ± 2.6	1.13 ± 0.15
37	94.08706	-21.3712	21 ± 6.3	7.6	32 ± 5.6	7.6 ± 4.4	-0.43 ± 0.31	5.8 ± 1.8	0.31 ± 0.09
38	94.08906	-21.3738	18 ± 6	6.1	11 ± 4.9	15 ± 4.4	-0.19 ± 0.35	5 ± 1.6	0.27 ± 0.09
39	94.09023	-21.3654	8.9 ± 4.8	3.7	2.2 ± 3.3	6.7 ± 4.2	0.51 ± 0.60	2.5 ± 1.3	0.13 ± 0.07
40	94.09177	-21.3727	350 ± 22	74	46 ± 9.4	300 ± 20	0.74 ± 0.05	97 ± 6	5.15 ± 0.32
41†	94.09429	-21.3608	70 ± 10	24	50 ± 8.8	20 ± 6.1	-0.44 ± 0.14	19 ± 2.8	1.03 ± 0.15
42	94.09447	-21.3773	10 ± 5.3	5.7	10 ± 4.7	4.5 ± 3.7	-0.38 ± 0.41	2.4 ± 1.5	0.21 ± 0.08
43	94.09474	-21.3783	13 ± 4.8	4.3	5.9 ± 4.3	4.5 ± 3.5	-0.18 ± 0.33	2.8 ± 1.3	0.15 ± 0.07
44	94.09764	-21.3741	9.6 ± 4.6	2.3	3.3 ± 2.3	6.3 ± 4.1	0.30 ± 0.53	2.9 ± 2.6	0.17 ± 0.07
45	94.09788	-21.3719	69 ± 10	20	37 ± 7.4	32 ± 7.1	-0.07 ± 0.11	14 ± 2.2	1.02 ± 0.13
46	94.09820	-21.3692	51 ± 9	5.4	30 ± 3.3	1.5 ± 2.9	-0.19 ± 0.37	14 ± 1.5	0.76 ± 0.13
47	94.09823	-21.3692	12 ± 5.5	5.4	13 ± 3.3	1.5 ± 2.9	-0.80 ± 0.37	4.1 ± 1.5	0.22 ± 0.08
48	94.09833	-21.3692	12 ± 5.5	5.4	13 ± 3.3	1.5 ± 2.9	-0.80 ± 0.37	4.1 ± 1.5	0.22 ± 0.08
49	94.10012	-21.3819	8.3 ± 4.6	3.6	3.5 ± 3.4	5.1 ± 4.7	0.31 ± 0.33	2.3 ± 1.5	0.25 ± 0.09
50	94.10064	-21.3819	41 ± 8	16	33 ± 3.3	12 ± 4.2	-0.64 ± 0.11	13 ± 2.2	0.62 ± 0.12
51	94.10071	-21.3865	44 ± 8.6	10	33 ± 3.3	12 ± 4.2	-0.47 ± 0.11	13 ± 2.2	0.65 ± 0.12
52	94.10097	-21.3622	24 ± 8.3	10	12 ± 7.5	12 ± 4.2	0.08 ± 0.28	7.1 ± 2.2	0.38 ± 0.14
53	94.10377	-21.3641	44 ± 8.6	10	33 ± 3.3	12 ± 4.2	-0.47 ± 0.11	13 ± 2.2	0.65 ± 0.12
54	94.10433	-21.3720	7.3 ± 4.3	19	34 ± 7.6	19 ± 9.4	-0.23 ± 0.17	16 ± 2.2	0.84 ± 0.14
55	94.10548	-21.3720	7.3 ± 4.3	19	34 ± 7.6	19 ± 9.4	-0.23 ± 0.17	16 ± 2.2	0.84 ± 0.14
56*	94.10608	-21.3733	24 ± 6.4	7.7	18 ± 3.3	5.3 ± 3.3	-0.55 ± 0.27	6.6 ± 1.7	0.35 ± 0.10
57	94.10637	-21.3704	20 ± 5.9	7	2.6 ± 3.3	5.3 ± 3.3	0.73 ± 0.30	5.5 ± 1.7	0.29 ± 0.09
58	94.10726	-21.3758	9 ± 4.7	3.6	4.5 ± 3.3	4.5 ± 3.3	-0.00 ± 0.59	3.6 ± 1.4	0.14 ± 0.07
59	94.10817	-21.3771	43 ± 8.1	15	25 ± 3.3	17 ± 4.7	-0.27 ± 0.20	12 ± 2.3	0.66 ± 0.12
60	94.10868	-21.3750	13 ± 9.1	4.9	7 ± 4.7	6.1 ± 3.9	-0.07 ± 0.43	3.9 ± 1.5	0.21 ± 0.08
61	94.10971	-21.3752	16 ± 9.3	6.9	12 ± 5.2	3.6 ± 3.9	-0.55 ± 0.38	4.5 ± 1.6	0.24 ± 0.09
62	94.11047	-21.3701	130 ± 11	60	83 ± 11	17 ± 3.3	-0.28 ± 0.10	36 ± 3.4	1.93 ± 0.20
63	94.11082	-21.3769	9.1 ± 4.7	4	7.3 ± 4.3	1.7 ± 3.3	-0.62 ± 0.55	2.7 ± 1.4	0.14 ± 0.07
64	94.11177	-21.3698	89 ± 11	27	60 ± 9.4	29 ± 6.8	-0.35 ± 0.12	26 ± 3.2	1.36 ± 0.17
65	94.11218	-21.3762	6.1 ± 4.1	2.4	0 ± 2.1	6.4 ± 4.7	1.00 ± 0.66	1.9 ± 1.2	0.10 ± 0.07
66	94.11240	-21.3632	31 ± 7.3	12	21 ± 6.2	9.8 ± 4.7	-0.37 ± 0.24	8.7 ± 2	0.46 ± 0.11
67	94.11423	-21.3713	22 ± 6.3	8	18 ± 5.8	4 ± 3.6	-0.64 ± 0.28	6.5 ± 1.8	0.35 ± 0.10
68	94.11599	-21.3825	9.5 ± 4.8	4	7.9 ± 4.4	1.6 ± 3.9	-0.65 ± 0.54	2.7 ± 1.4	0.14 ± 0.07
69	94.11693	-21.3759	8 ± 4.5	3.1	6 ± 4.2	2 ± 2.9	-0.49 ± 0.60	2.3 ± 1.3	0.12 ± 0.07
70	94.11814	-21.3609	79 ± 11	29	53 ± 8.8	26 ± 6.6	-0.35 ± 0.13	23 ± 3	1.21 ± 0.16
71	94.12022	-21.3768	9.8 ± 4.7	3.9	8 ± 4.4	1.8 ± 2.9	-0.63 ± 0.51	3.4 ± 1.6	0.18 ± 0.09
72	94.12192	-21.3680	30 ± 7	13	29 ± 6.8	0.95 ± 2.6	-0.94 ± 0.17	10 ± 2.3	0.54 ± 0.12
73	94.12476	-21.3786	39 ± 7.9	14	25 ± 6.6	14 ± 5.2	-0.28 ± 0.21	12 ± 2.4	0.64 ± 0.13
74	94.12505	-21.3792	46 ± 8.5	16	31 ± 7.8	8 ± 3.8	-0.42 ± 0.15	13 ± 2.4	0.71 ± 0.13

NOTE. — (1) Source number. (2) Right Ascension (RA). (3) Declination (Dec). (4) Net counts in broad (0.5–8 keV) band. The uncertainty expressed here takes into account the fluctuations in the source as well as in the background. (5) Broad band source detection significance from *wavdetect*. This computes how unlikely it is for the background in the customized psf region to fluctuate to yield the detected number of counts. Note that the psf region is optimized differently in *wavdetect* than in the calculation of column (4) and is typically larger than in the latter. (6)–(7) Net counts in soft (0.5–2 keV) and hard (2–8 keV) bands respectively. Uncertainties in net counts are quoted to 1 σ . (7) Hardness ratio, computed with eq. (1). Uncertainties were obtained by applying error propagation to the uncertainties in the net counts. (8) X-ray luminosity in the 0.5–8 keV band, (9) X-ray flux in the 0.5–8 keV band. † Central Active Galactic Nucleus, ‡ Extended soft X-ray source, * SN 2003H (3.1'' match), ◇ SN 2013ai (0.12'' match), * SN 1999ec (4.2'' match).